Enhancement of the electrocatalytic activity of phthalocyanines through the reduction in symmetry and conjugation to detonation nanodiamonds

A thesis submitted in fulfilment of the requirements for the degree

of Master of Science

Of Rhodes University

By

Lunathi Ncwane

February 2023

Table of Contents

Dedication.....v

Acknowledgements.....vi

Abstract.....vii

List of abbreviations.....viii

List of symbols.....x

Preface.....xi

Chapter 1

1 INTRODUCTION 1

1.1 Detonation Nanodiamonds (DNDs) 2

1.2 Phthalocyanines (Pcs) 4

1.2.1 Synthesis 5

1.2.2 Electronic spectra of phthalocyanines 8

1.2.3 Phthalocyanines employed in this work (All new) 9

1.3 Electrocatalysis 15

1.3.1 Overview 15

1.3.2 Electrode modification methods 16

1.3.3 Phthalocyanines in electrocatalysis 18

1.3.4 Detonation nanodiamonds in electrocatalysis 19

1.4 Analyte 20

1.5 Summary of Aims and Objectives 21

Chapter 2

2 MATERIALS, EXPERIMENTAL AND EQUIPMENT. 22

2.1 Materials 23

2.2 Equipment 23

2.3 Synthesis 24

2.3.1 Synthesis of Complex 1, Scheme 3.1 24

2.3.2 Synthesis of Complex 2, Scheme 3.2 25

2.3.3 π-π stacking of complexes 1 and 2 onto DNDs, Scheme 3.3 25

2.3.4 Covalent linkage of complex 2 to DNDs, Scheme 3.4 26

2.4 Electrode modification 26

Chapter 3

3 CHARACTERISATION 28

3.1 Characterisation of the MPcs 29

3.2 Characterisation of MPc-DNDs composites 33

3.2.1 UV-visible spectra 36

3.2.2 FT-IR 37

3.2.3 TEM and DLS 38

3.2.4 Raman spectroscopy 40

3.3 Summary of the chapter 43

Chapter 4

4 ELECTRODE CHARACTERISATION 44

4.1 Studies in ferricyanide 45

4.1.1 Cyclic voltammetry 45

4.1.2 Chronocoulorimetry 47

4.1.3 Electrochemical impedance spectroscopy 49

4.2 Cyclic voltammetry in sodium hydroxide 53

4.3 Summary of the chapter 56

Chapter 5

5 HYDRAZINE ELECTROCHEMICAL SENSING 57

5.1 Cyclic voltammetry 58

5.2 Kinetics 63

5.3 Stability studies 66

5.4 Chronoamperometry 67

5.5 Interference studies 72

5.6 Summary of the chapter 74

Chapter 6

6 CONCLUSIONS AND FUTURE ASPECTS 75

6.1 Conclusions 76

6.2 Future aspects 76

Dedication

This is dedicated to my parents Mphuthumi and Buziwe Ncwane, my siblings Bukho, Lihle and Yonelisa.

Acknowledgements

To my supervisor, Distinguished Professor Tebello Nyokong who made this MSc journey a success. I am grateful for giving me the opportunity and believing in me.

I am thankful to my mentor, Dr Lekhetho Mpeta for your guidance. Extending my gratitude to Gail, Dr J Britton, Papa Francis, Prof J Mack, chemistry department and my s22 labmates.

To my family and friends, thank you for the support and encouragement.

Thank you to Rhodes University and Institute for Nanotechnology and Innovation. Financial support from the National Research Foundation (NRF) of South Africa through DST/NRF South African Research Chairs Initiative for Professor of Medicinal Chemistry and Nanotechnology (UID 62620) is gratefully acknowledged.

Abstract

This thesis reports on the synthesis of novel phthalocynines tetrakis[(benzo[d]thiazol-2ylthio)phthalocyaninato]cobalt(II)chloride (complex **1**) and tris(2-(ethylthio)benzo[d]thiazole)2-(phthalocyanine-9-ylthio)propionate cobalt(II) chloride (complex **2)**. The complexes are combined with DNDs via different techniques such as π-π stacking, covalent linkage and sequential modification on glassy carbon electrode. The synthesized MPcs and conjugates were characterized using UV-visible, mass, Fourier transform infrared, and Raman spectroscopies as well as transmission electron microscopy and dynamic light scattering. Combining MPcs with DNDs sought to improve electrooxidation of hydrazine. The electrochemical studies were conducted using cyclic voltammetry, chronocoloumetry, electrochemical impedance spectroscopy and chronoamperometry. Hydrazine was utilized as an analyte of interest, due to its mutagenic and carcinogenic effects. Glassy carbon electrodes (GCE) were modified using drop and dry method. The conjugation via covalent linkage proved to be the best way of enhancing electrocatalytic properties. Since it performed better in terms of limit of detection (0.33 μM), even though catalytic rate and sensitivity are not the highest.

List of abbreviations

CDs	Carbon dots
CV	Cyclic voltammetry
DCC	Dicyclohexylcarbodiimide
DHP	Dihexadecyl phosphate
DLS	Dynamic light scattering
DMF	Dimethylformamide
DMSO	Dimethylsulfoxide
DNDs	Detonation nanodiamonds
FT-IR	Fourier transform-infrared
GCE	Glassy carbon electrode
GQDs	Graphene quantum dots
g-C_3N_4	Graphitic carbon nitride,
LoD	Limit of detection
MALDI-TOF	Matrix assisted laser-desorption/ionization-time of flight
NDG/CS	Nanodiamond-graphite/chitosan
Nd:YAG	Neodymium-doped yttrium aluminum garnet
NLO	Nonlinear optics
NMR	Nuclear magnetic resonance
PACT	Photodynamic-antimicrobial chemotherapy

PDT	Photodynamic therapy
Pc(s)	Phthalocyanine(s)
rGONs	Reduced graphene oxide nanosheets
TEM	Transmission electron microscopy
UV-vis	Ultraviolet-visible

List of symbols

k_{cat}	Catalytic rate constant
R_{ct}	Charge transfer resistance
C	Concentration
K	Constant
I_{buf}	Currents in the absence of analyte
I_{cat}	Currents in the presence of analyte
D	Diffusion coefficient
A	Electrode surface area.
F	Faraday's constant
I_D	Intensity of Raman D band
I_G	Intensity of Raman G band
α	Non-peripheral position
ß	Peripheral position
ΔE_p	Peak potential separation
Γ	Surface coverage
δ	Standard deviation
b	Tafel slope

Preface

The research on the determination of harmful substances in the environment and humans is of interest to many researchers. Hydrazine is one of the widely studied analytes due to its toxicity which causes severe damage to the central nervous system, kidneys and liver. Development of electrocatalysts is of interest in this work for the detection of hydrazine. Phthalocyanines of different symmetry are employed in this thesis and their electrocatalytic properties enhanced by detonation nanodiamonds. Enhancement of phthalocyanine's electrochemical properties using zero-dimensional carbon allotropes such as graphene quantum dots and carbon dots have been reported. However, this is the first time that detonation nanodiamonds are incorporated to phthalocyanines for electrocatalysis.

1 INTRODUCTION

This chapter reviews literature on detonation nanodiamonds, phthalocyanines, electrocatalysis, the analyte and electrode modification employed in this work.

1.1 Detonation Nanodiamonds (DNDs)

Diamonds may be called a "supermaterials" according to Spitsyn and Alexenko [1], since they exhibit fascinating physical, mechanical and chemical properties that are more superior compared to other materials [2]. The utilization of diamonds in science over the years has been of great interest. One of the major and growing applications is in nanotechnology through miniaturization of the bulk diamond to diamond nanoparticles (nanodiamonds), hence improving the already exciting properties of the natural diamond [3]. These types of nanomaterials do not only show diamond properties which include high thermal conductivity and hardness, but also possess unique nanomaterial properties such as large surface area, small particle size and large numbers of surface defects [4,5]. Nanodiamonds belong to a group of zero-dimensional carbon allotropes which include graphene quntum dots and carbon dots. Zero-dimensional carbon allotropes have tunable properties and nanodiamonds are no exception. The tuning of nanodiamonds include doping, and surface functionalization, this enables application in various fields such as drug delivery [6], sensing [7], bioimaging [8], catalysis [9], energy storage [10], photovoltaics [11], etc. Some of the applications of nanodiamonds are displayed in **Fig. 1.1** [12].

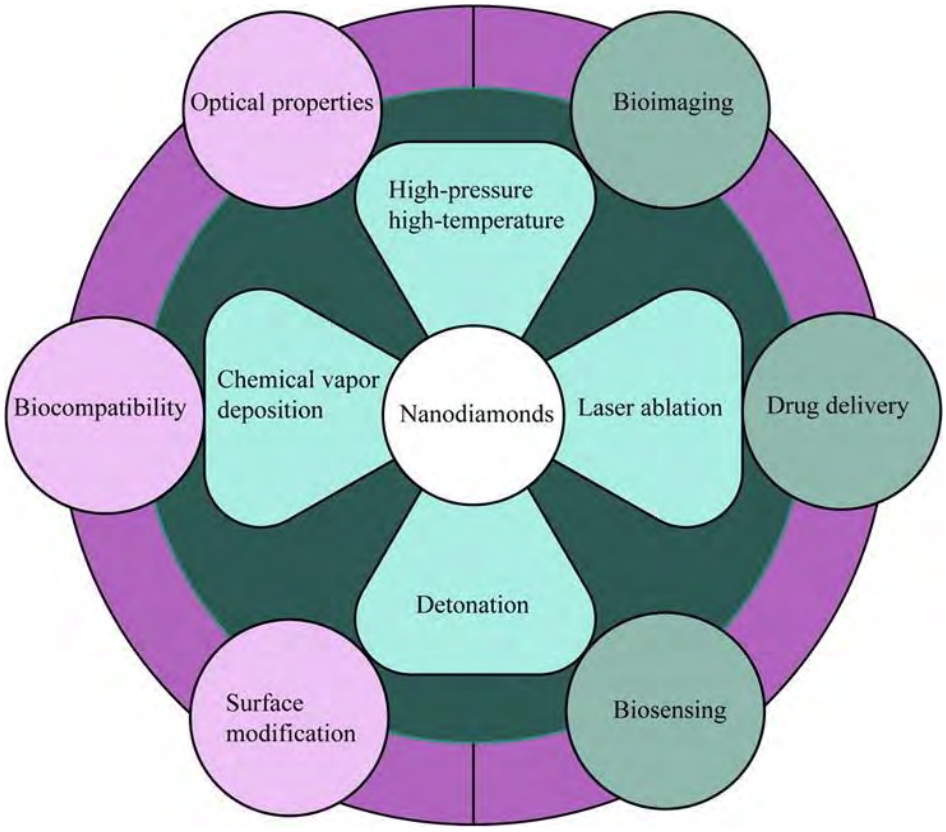

Figure 1.1: Synthetic techniques, properties and various applications of nanodiamonds **[12]**.

Diamond nanoparticles are widely synthesized using a process called detonation, hence the name detonation nanodiamonds (DNDs) and are used in this work. Detonation nanodiamonds, also known as ultra-dispersed diamonds (UDD) are novel carbon nanomaterials made up of a tetrahedral network structure, and comprise a diamond core (sp^3), a middle core (sp^2+x) and a graphitized outer layer (sp^2) which are often partially oxidized, **Fig. 1.2 [13]**. The presence of π electrons allows for π-π stacking with other materials with π electron system. In addition, DNDs are made up of several functional groups on the surface such as amine, alcohol, and carboxyl, illustrated in **Fig. 1.2 [14,15]**, which allow for covalent linkage of the DNDs to different materials such as phthalocyanines. The incorporation of nanomaterials

with porphyrins and phthalocyanines, seeks to enhance the properties of the latter [16,17].

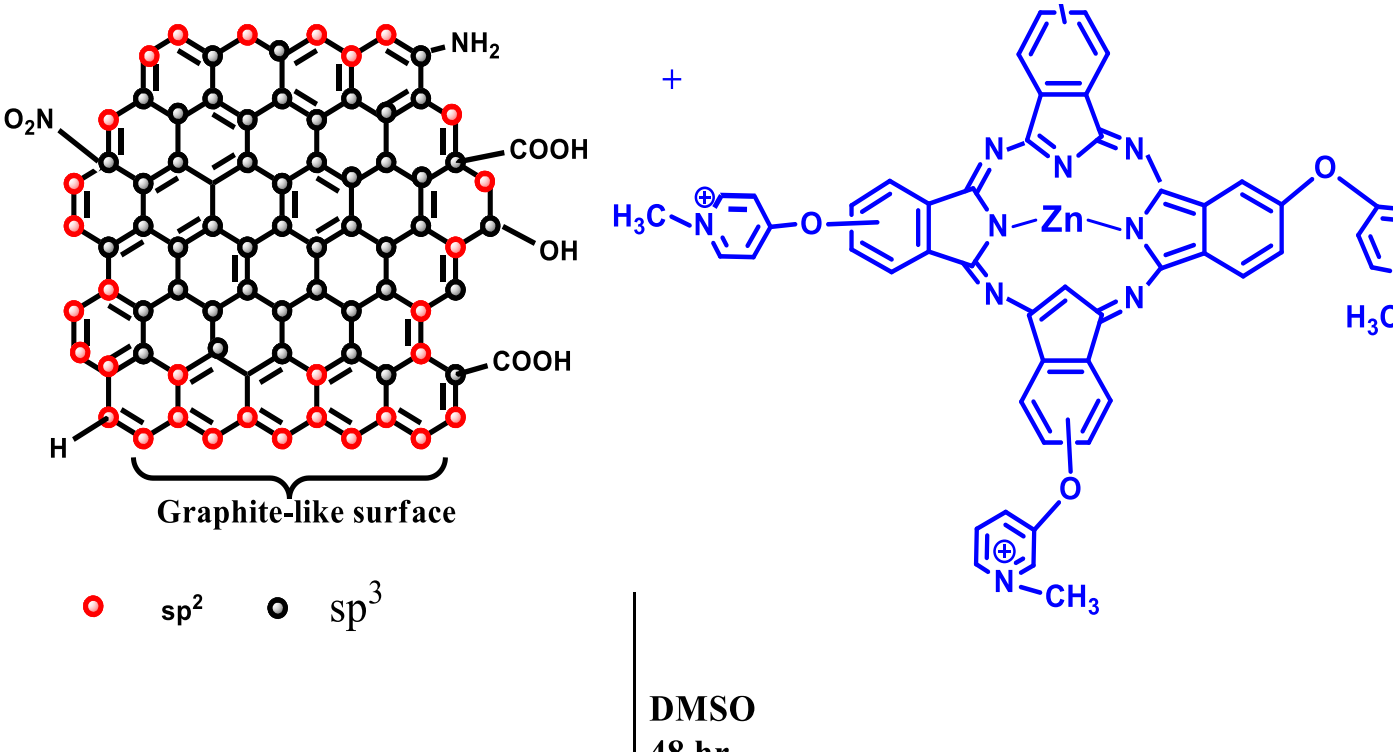

Figure 1.2: A typical structure of detonation nanodiamonds **[18].**

1.2 Phthalocyanines (Pcs)

Research on phthalocyanines has been ongoing for many years. Throughout the years, researchers have been investigating ways of improving the chemical properties of the phthalocyanines. Activity and properties of the Pc can be enhanced by introducing different central metals and substituents of the ring at the peripheral (α-alpha) and non-peripheral (β-beta) positions of the ring, **Fig. 1.3.** Phthalocyanines are chemically flexible, which permits their modification to suit specific applications **[19]**. Phthalocyanines have been widely applied in photodynamic therapy (PDT) as photosensitizers, solar cells, sensing and catalysis, and in non-linear optics to name a few **[20-23]**.

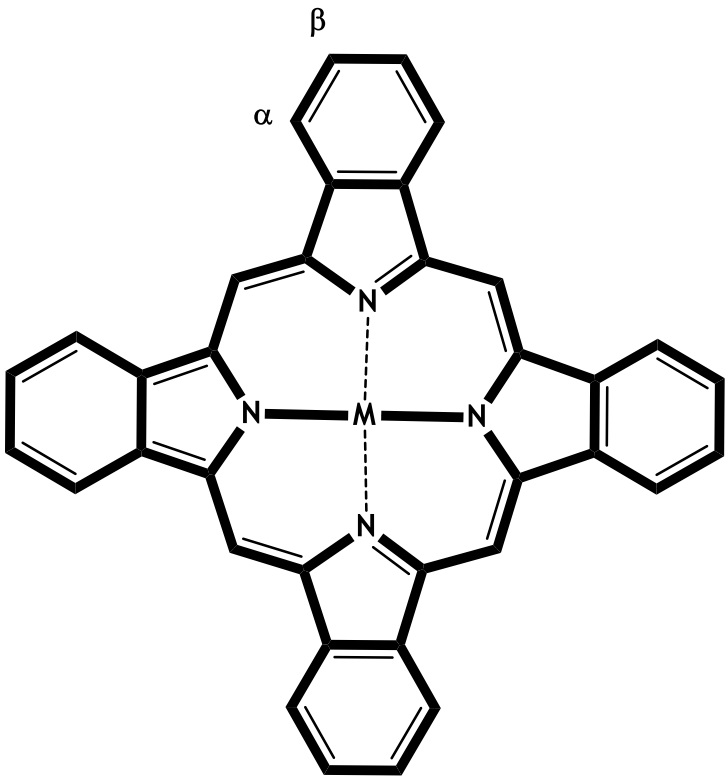

Figure 1.3: Molecular structure of the MPc illustrating peripheral (α-alpha) and non-peripheral (β-beta) positions.

1.2.1 Synthesis

Synthesising metallophthalocyanines (MPcs) involves the utilization of precursors such as phthalonitrile, phthalamide, phthalic anhydride, phthalic acid, phthalimide, o-cyanobenzamide or 1.3-diiminoisoindoline, metal salts and a catalyst, **Scheme 1.1**. Phthalonitriles are mostly used in the laboratory. There are two types of MPcs (symmetrical and asymmetrical). The symmetrical MPcs can be synthesised from one phthalonitrile, whereas asymmetrical involves two different phthalonitiles, polymer support and the sub-phthalocyanine approach **[24,25]**. The synthesis is usually carried out by cyclotetramerization of phthalonitriles under high temperature conditions **[26]**.

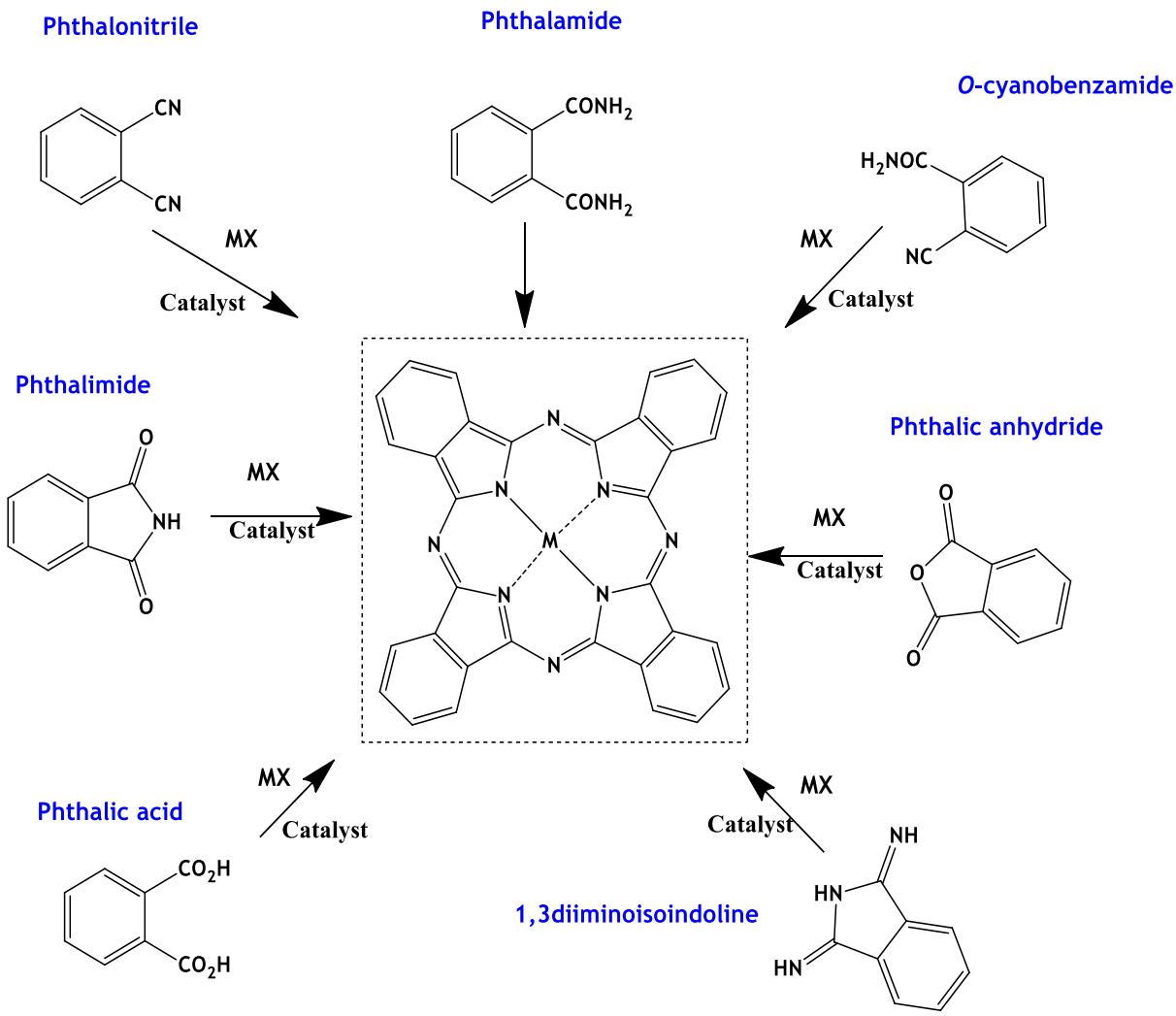

Scheme 1.1: Various starting materials for the synthesis of metallophthalocyanines (MX = metal salt).

1.2.1.1 Asymmetrical MPcs

The synthesis of mono substituted MPcs (AAAB or ABBB) (asymmetrical Pc), **Scheme 1.2**, involves the combination of two different phthalonitriles depending on the type of application. This is achieved by following the widely used statistical condensation

approach with ratios such as 1:3, 1:5 and 1:9. However, 1:3 ratio is the most preferred and employed in this thesis, since it limits the formation of tetrasubstituted MPcs. The formed product is usually a mixture of different isomers (**Scheme 1.2**), which can be separated by column chromatography to get the desired complex.

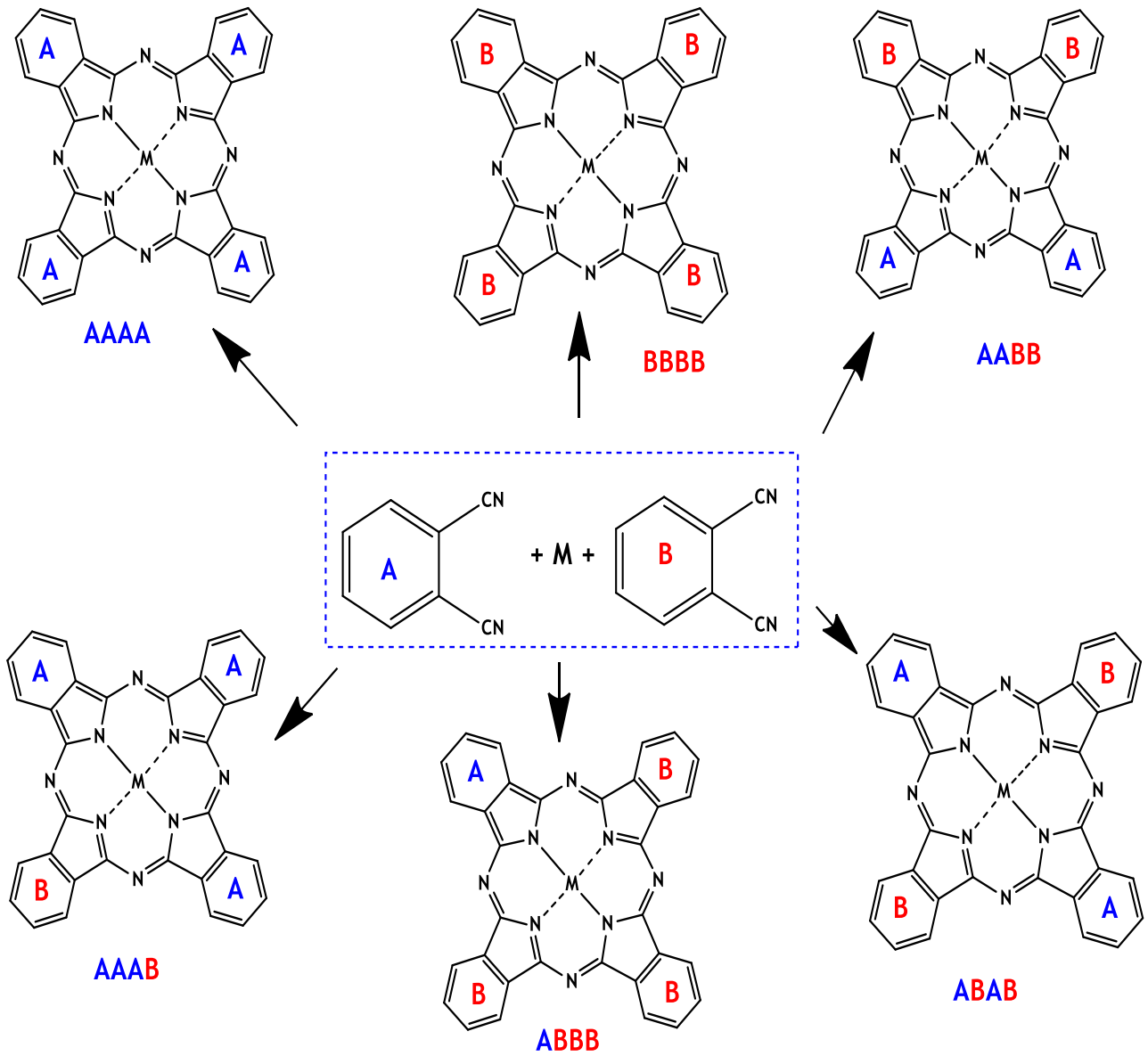

Scheme 1.2: Synthesis of asymmetrical metallophthalocyanines.

1.2.1.2 Symmetrical MPcs

The synthesis of symmetric MPcs involves one type of phthalonitrile, **Scheme 1.3**. When compared to the asymmetrical MPcs, symmetrical phthalocyanines give better yields.

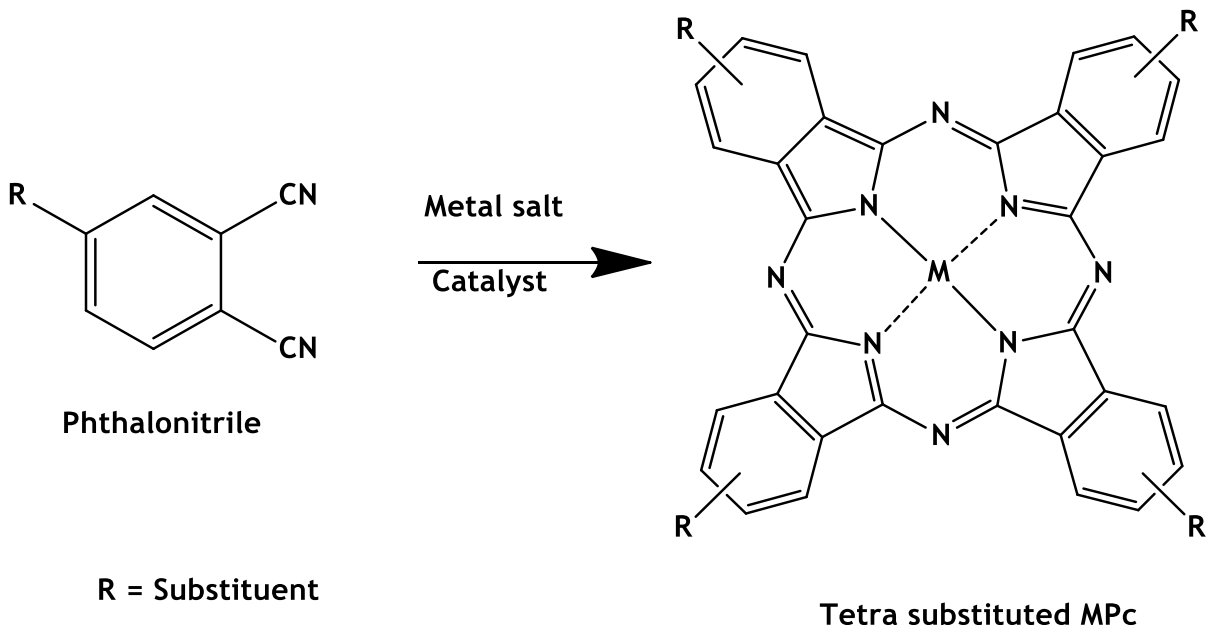

Scheme 1.3: Synthesis of symmetric (tetra substituted) MPcs.

1.2.2 Electronic spectra of phthalocyanines

The electronic spectra phthalocyanines consists of the Q and B bands. The Q-band is observed at 650 nm or longer, whereas B-band is observed at 300 nm – 400 nm. **Figure 1.4** shows an electronic absorption spectra and electronic energy levels of the phthalocyanine. The positions of the Q and B bands are determined by the type of substituent, central metal, conjugation to nanomaterials, or symmetry **[27,28]**.

These induce red or blue shifts on the Q – band. The Q-band is associated with a_{1u} to e_g transitions while the B-band(s) is due to b_{2u} and a_{2u} to e_g transition, which are due to π-π^* transitions occurring in the phthalocyanine ring **[28]**.

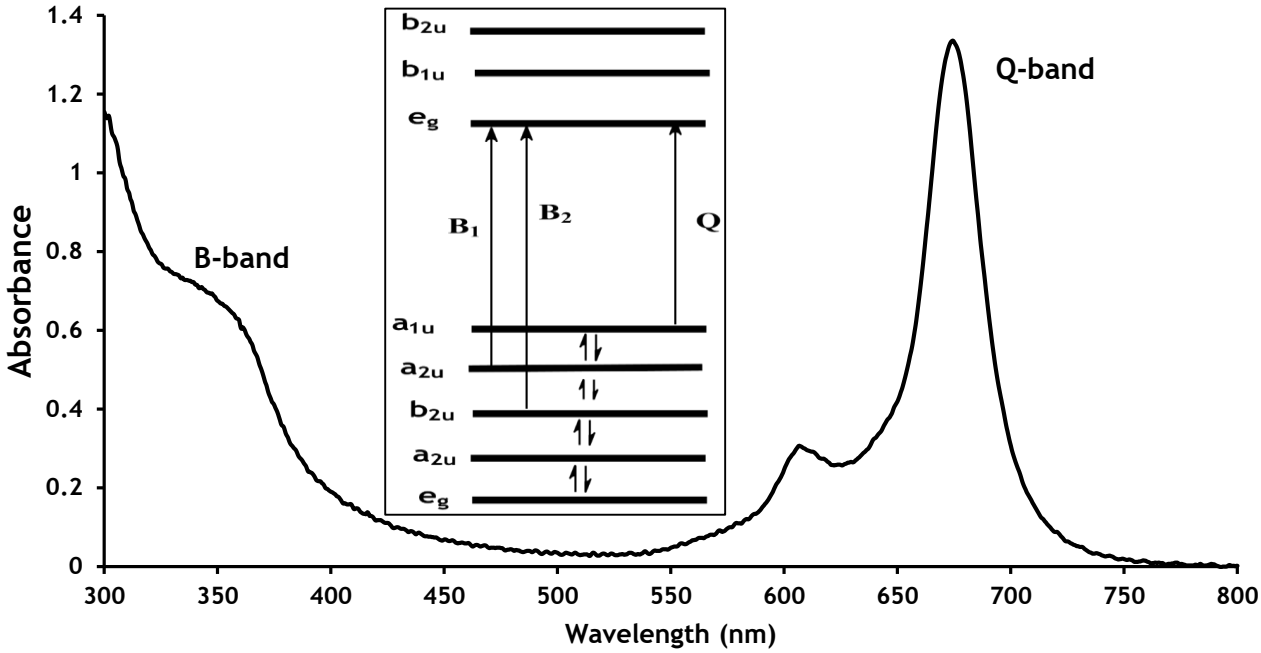

Figure 1.4: Electronic absorption spectra of a typical phthalocyanine and electronic energy levels (insert).

1.2.3 Phthalocyanines employed in this work (All new)

The structures of symmetrical (**complex 1**) and asymmetrical (**complex 2**) metallophthalocyanines employed in this thesis, are shown in **Table 1.1**. The complexes are made up of benzothiazole and mercaptopropionic acid substituents and cobalt as a central metal. In this work symmetrical MPc **complex 1** is employed in combination with detonation nanodiamonds (DNDs) via π-π stacking as an electrocatalysts for hydrazine. The ring for **complex 1** has been reported for central metals such as Ga and Zn **[29]**, but it is reported for the first time for Co as a central

metal in this work. In addition, asymmetrical **complex 2** made up of benzothiazole and mercaptopropionic acid is also reported for the first time in this thesis.

The benzothiazole substituents found in both complexes are known electrocatalyst **[30-32]**. The quest for improving the properties of the phthalocyanine has been ongoing for decades. In this work benzothiazole substituents is utilised to improve the π-conjugated system of the Pc, since benzothiazoles possess large conjugated system **[33]**. In addition, benzothiazole is an electron donating group and thus make the MPc complexes more readily oxidised **[34]** and improves the solubility of the complex.

Complex 2, an asymmetrical phthalocyanine, contains mercaptopropionic acid as one of the substituents. The COOH functional group in mercaptopropionic acid is used for covalent linkage via amide bond with DNDs.

The investigation of the electrocatalytic activity of symmetrical and asymmetrical phthalocyanines has been reported over the years **[35-37]**. However, symmetrical Pcs are the most studied due to their ease of synthesis. The asymmetrical phthalocyanines are known to possess good non-linear optical and recently electrocatalytic properties when compared to symmetrical derivatives **[38,39]**. **Table 1.2**, shows Pcs which have been linked to zero dimensional carbon based nanomaterials **[40-49].**

Table 1.1: MPcs and MPc-DNDs composites employed in work for electrocatalysis of hydrazine.

MPc structure	MPc-DNDs hybrids
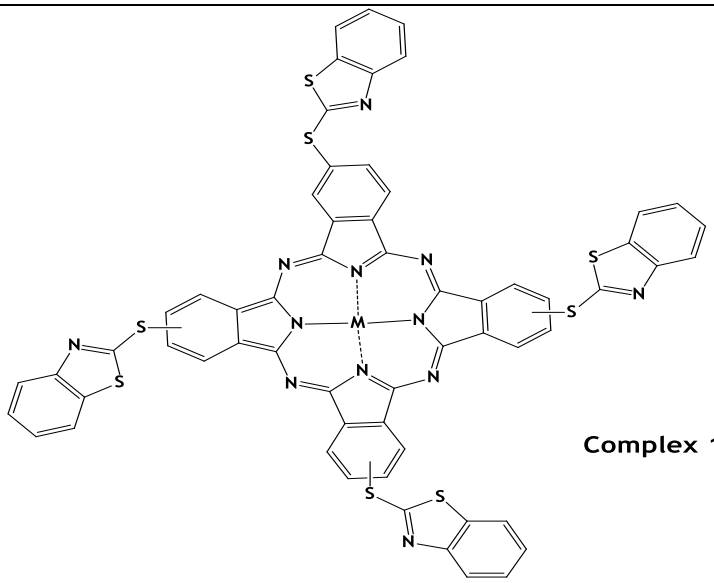 Complex 1 **Tetrakis[(benzo[d]thiazol-2ylthio)phthalocyaninato]cobalt(II)chloride**	DNDs ππ stacked with **complex 1** (**1-DNDs(ππ)**). **(New)**
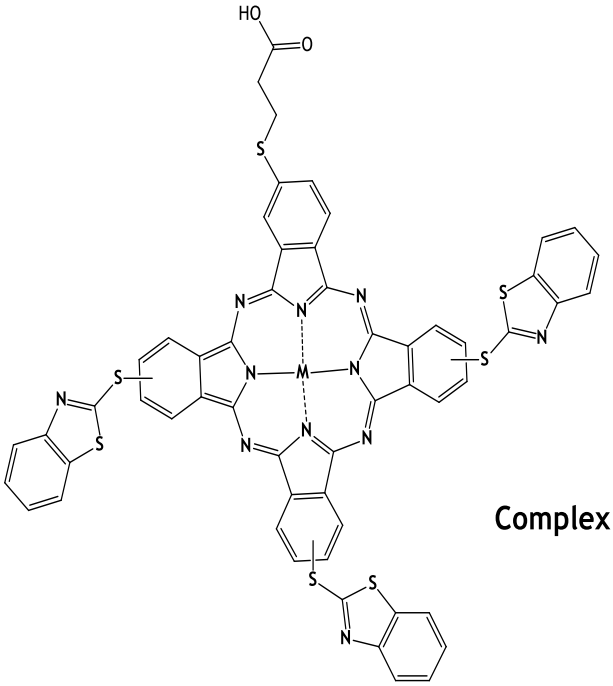 Complex 2 **Tris(2-(ethylthio)benzo[d]thiazole)2-(phthalocyanine-9-ylthio)propionate cobalt(II) chloride**	DNDs ππ stacked (**2-DNDs(ππ)**) and covalently linked (**2@DNDs**) with **complex 2** **(New)**

Table 1.2: Shows zero-dimensional carbon allotropes (carbon dots (CD), detonation nanodiamonds (DNDs), and graphene quantum dots (GQDs)) conjugated to MPcs for various applications.

Carbon nanomaterial	MPc structure	Application/Analyte	Nanomaterial-MPc interaction	References
NGQDs NSGQDs	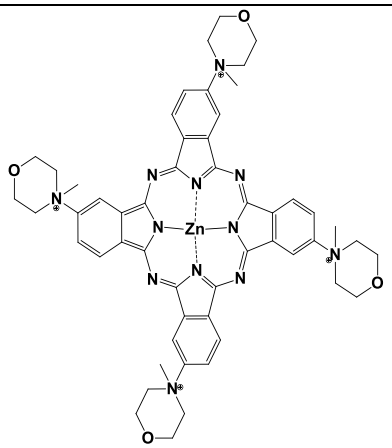	Photo-sonodynamic therapy	π-π stacking	[40]
DNDs	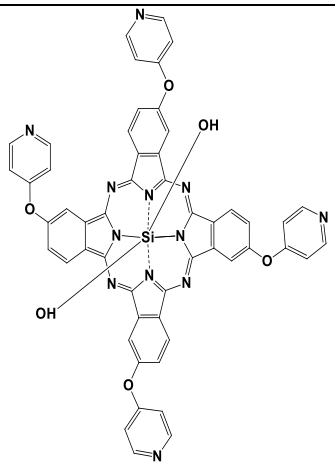	Photophysics and Non-Linear Optics (NLO)	Axial ligation	[41]

NCDs	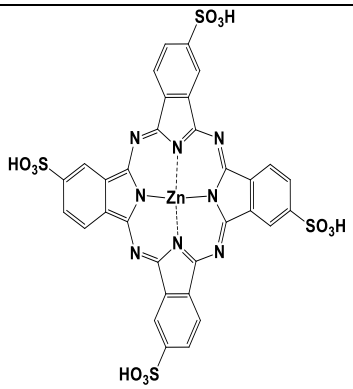	Dye-sensitised solar cells (DSSCs)	π-π stacking	[42]
CDs	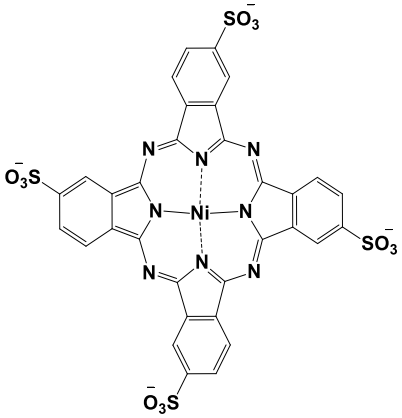	Photophysics	π-π stacking	[43]
GQDs	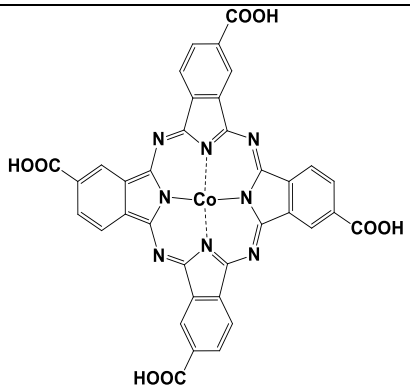	Gas sensing	π-π stacking	[44]
GQDs	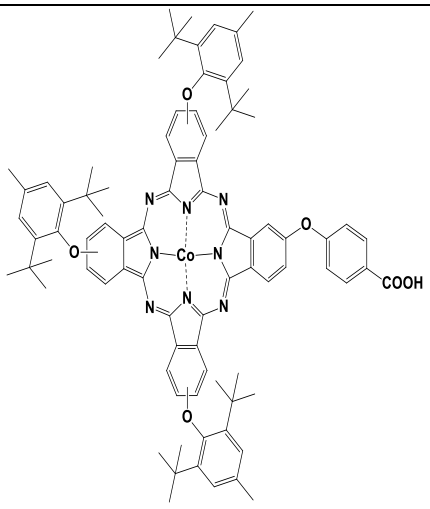	Electrochemical biosensing	π-π stacking	[45]

g-C_3N_4/GQDs	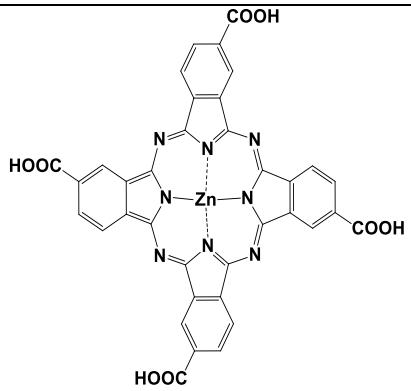	Photodegradation	Covalent linkage	[46]
DNDs	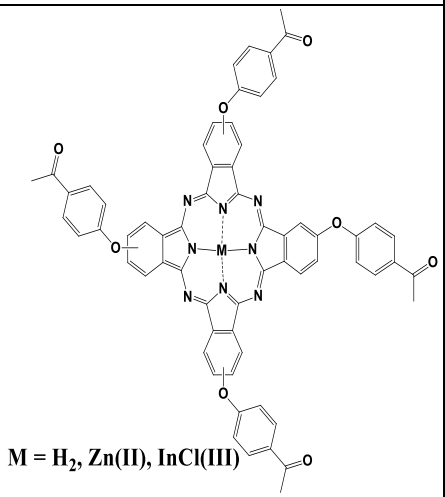	Photodynamic-antimicrobial chemotherapy	π-π stacking	[47]
GQDs	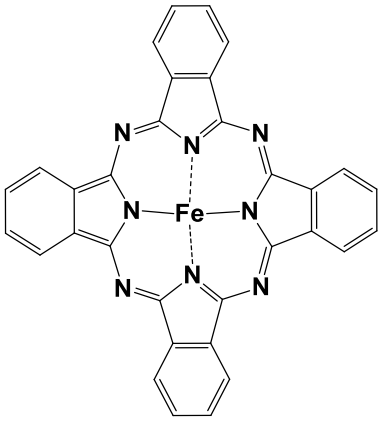	Oxygen reduction reaction (ORR)	GQDs linked axially using Fe-O bonds	[48]
N, S-CDs	CuPc derivative (structure not shown)	Photoelectrochemical biosensing	Electrostatic adsorption	[49]

NGQDs = nitrogen doped graphene quantum dots, **NSGQDs** = nitrogen-sulfur doped graphene quantum dots, **NCDs** = nitrogen doped carbon dots, **CDs** = carbon dots, **GQDs** = graphene quantum dots, **g-C_3N_4** = graphitic carbon nitride, **N, S-CDs** = nitrogen-sulfur doped carbon dots.

Conjugation of detonation nanodiamonds to Pcs is shown in **Table 1.2** for non-linear optics and photodynamic-antimicrobial chemotherapy (PACT) applications. But there is no reported work for applications in electrochemical sensing, hence the interest in this thesis **[40-49]**.

1.3 Electrocatalysis

1.3.1 Overview

Electrocatalysis, may be described as an improvement of the rate of an electrochemical reaction in the presence of a catalyst. Electrocatalysis has been widely used in research and industry for various applications **[50]**. One of exciting applications, is in electrochemical sensing **[51]**. Electrochemical sensing is a detection technique, where an electrocatalyst is employed. In this case, electrocatalysts catalyse the redox reactions occurring at the working electrode's surface. Electrocatalysts can reduce the catalytic potential and increase the currents **[52]**. **Fig. 1.5** illustrates an impact of electrocatalyst when it is introduced to the surface of a bare electrode **[53]**.

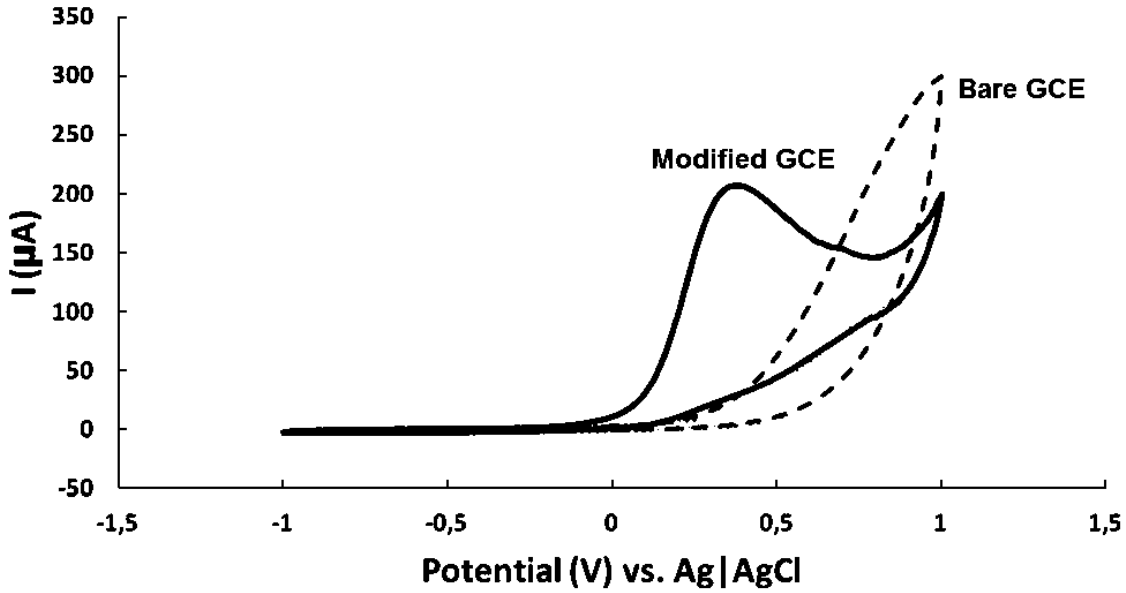

Figure 1.5: Comparative cyclic voltammograms of a modified glassy carbon electrode (GCE) and a bare GCE in 6 mM of hydrazine (0.2 M NaOH) **[53]**.

1.3.2 Electrode modification methods

Various modification approaches have been developed including the following: electrochemical grafting, adsorption, electrodiposition and self-assembly, etc. Herein, adsorption 'drop and dry' is employed, **Fig. 1.6 [54]**.

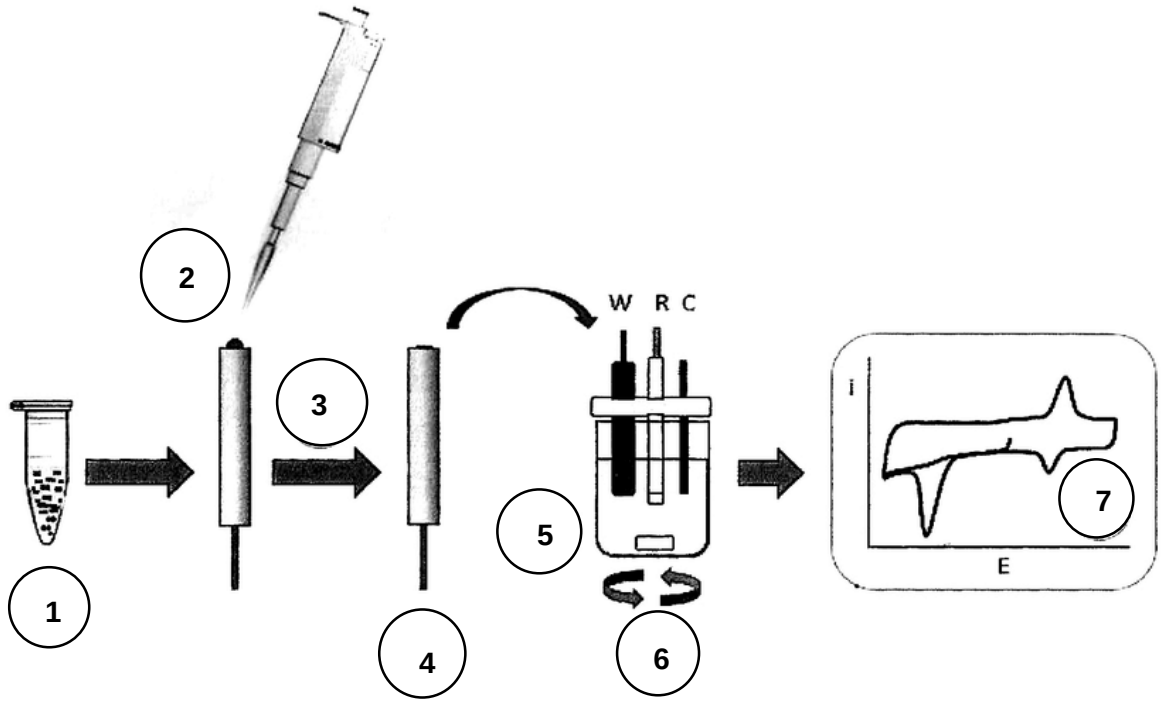

Figure 1.6: Illustration of the 'drop and dry' modification of electrodes (1-4), electrochemical cell setup (5 and 6), and electrochemical characterisation and sensing plot (7) **[54]**.

This method involves physically adsorbing the electrocatalyst by dropping it on electrode's surface. The physical adsorption method involves dissolving the MPc or nanomaterials in a suitable solvent, and dropping a known amount on the surface, **Fig. 1.6**. Drop and dry method is simple and time saving. The π electron system found in phthalocyanines and zero-dimensional carbon allotropes such as DNDs, GQDs and CDs informed the utilization of the glassy carbon electrode. The materials may interact with the π system of the glassy carbon electrode forming stable layers.

1.3.3 Phthalocyanines in electrocatalysis

MPcs serve as electron mediators in electrocatalysis, due to fascinating redox chemistry **[55]**. The electron mediation depends on the type of a central metal or substituents on the Pc ring. Electroactive central metals are the most preferred as to enhance the already good electron transfer abilities of phthalocyanines. The widely used central metals arranged in order electrocatalytic activity include: Fe^{2+} > Co^{2+} > Mn^{2+} > Ni^{2+} ≈ Cu^{2+}, with Fe^{2+} and Co^{2+} being the most active and extensively explored in electrocatalysis **[56]**. **Fig. 1.7** illustrates the electron transfer process occurring on electrode's surface for the central metal (M^{II}/M^{III} redox couple) **[57]**.

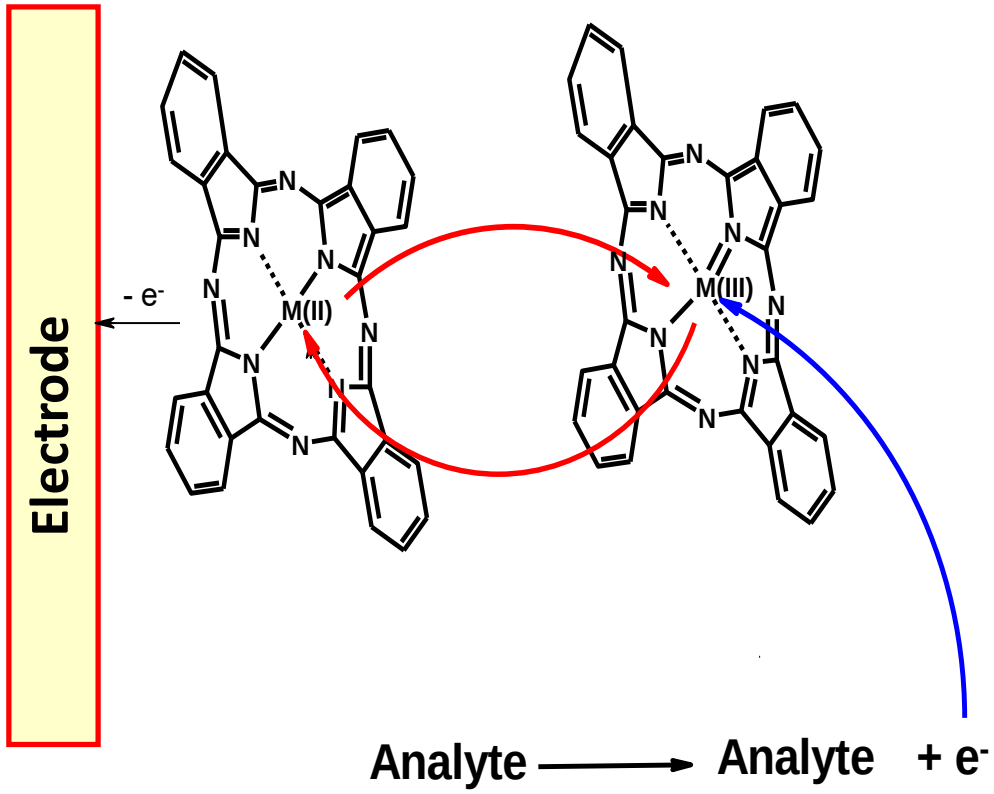

Figure 1.7: An electrocatalytic process of MPc on working electrode's surface **[57]**.

1.3.4 Detonation nanodiamonds in electrocatalysis

Carbon nanomaterials are known in electrocatalysis when employed alone, modified from their pristine state and in the presence of other materials such as phthalocyanines. Detonation nanodiamonds, have been used as supports for CO gas electrochemical sensing **[58]**. The functional groups present of DNDs surface enables modification and conjugation to other materials for the enhancement of properties **[59]**. **Table 1.3 [60-63]**, illustrates examples of use of some nanodiamonds for electrochemical sensing of various analytes. Due to their superior properties, nanodiamonds have been reported as good electrocatalysts in electrochemical sensing, because of low limits of detections (LoDs) obtained.

Table 1.3: DNDs based electrocatalysts in electrochemical sensing

Electrode	Analyte	Reference
ND/GCE	Pyrazinamide antibiotic	**[60]**
NDG/CS/GCE	Azathioprine	**[61]**
ND-DHP/GCE	Codeine	**[62]**
ND powder electrode	Nitrite	**[63]**

NDG/CS = Nanodiamond-graphite/chitosan, **DHP** = Dihexadecyl phosphate.

1.4 Analyte

Hydrazine was employed as a test analyte in this work. Hydrazine is useful in various industries such as agriculture, pharmaceuticals, and as rocket fuel. At high concentrations it can be harmful to living organisms and humans, hence the need for constant detection **[64,65]**. Several techniques have been developed for the detection of hydrazine such as spectrometry, chromatography and chemiluminescence. However, these have too many disadvantages such as, time consuming due to sample pre-treatments, require complicated and costly equipment and poor stability **[66,67]**. The electrochemical methods are preferred due to high sensitivity, low limits of detection, cost effectiveness **[68,69]**.

The mechanism of hydrazine as an analyte, using electrocatalyst (CoPc as an example) is as follows **[70] eqns 1.1-1.4**:

$$[Co(I)Pc]^- \longleftrightarrow [Co(II)Pc] + e^- \qquad \textbf{(1.1)}$$

$$[Co(II)Pc] + N_2H_4 + OH^- \xrightarrow{RDS} [Co(I)Pc\ldots N_2H_3]^- \qquad \textbf{(1.2)}$$

$$[Co(I)Pc\ldots N_2H_3]^- \longrightarrow [Co(I)Pc]^- + {}^*N_2H_3 \qquad \textbf{(1.3)}$$

$${}^*N_2H_3 + 3OH^- \xrightarrow{fast} N_2 + 3e^- + 3H_2O \qquad \textbf{(1.4)}$$

RDS = Rate Determining Step

1.5 Summary of Aims and Objectives

The main aim of the work in this thesis is to design new electrocatalysts for the electrochemical detection of hydrazine. This is conducted by altering the surface of the bare glassy carbon electrode. Nanodiamonds are employed to enhance the electrochemical properties of the symmetrical and unsymmetrical cobalt phthalocyanines via π-π stacking and covalent linkage.

The objectives of this thesis are:

- Synthesis of the novel cobalt phthalocyanines
- π-π stacking of the detonation nanodiamonds onto complexes **1** and **2.**
- Covalent linkage of detonation nanodiamonds and complex **2** via the amide bond
- Characterisation of the complexes and conjugates
- Investigate electron transfer abilities of the electrodes using cyclic voltammetry and electrochemical impedance spectroscopy (EIS) in 0.1 M KCl containing 1 mM $[Fe(CN)_6]^{3-/4-}$.
- Investigate the electrocatalytic properties of the modified electrodes towards hydrazine using cyclic voltammetry, chronocoulometry, and chronoamperometry.

2 MATERIALS, EXPERIMENTAL AND EQUIPMENT.

This chapter gives materials and equipment, also outlines synthesis of the phthalocyanines and conjugates, and electrode modifications employed in this thesis

2.1 Materials

Cobalt chloride, potassium chloride (KCl), iron ferricyanide, aluminium oxide, dicyclohexylcarbodiimide (DCC), were purchased from Sigma-Aldrich. Dimethylsulfoxide (DMSO), dimethylformadide (DMF), 1-pentanol, tetrahydrofuran (THF), 1,8-diazabicylo [5.4.0]-undec-7-ene (DBU), and methanol were purchased from Merk. Detonation nanodiamonds (DNDs) were obtained from Nanocarbon Research Institute Ltd.

2.2 Equipment

- UV-visible spectra data was obtained from Shimadzu UV–Vis 2550 spectrophotometer in the range of 300-800 nm.
- The mass spectra data was obtained on a Bruker AutoFLEX III Smart-beam TOF/TOF mass spectrophotometer using α-cyano-4-hydrocinnamic acid/THF as the matrix in the positive ion mode
- Elemental analysis was done using Vario-Elementer Microcubes ELIII.
- Infrared spectroscopy was performed using a Bruker Alpha IR (100 FT-IR) spectrophotometer.
- Transmission electron microscopy (TEM) images were obtained from Zeiss Libra TEM 120 model.
- Dynamic light scattering (DLS) was done on Malvern Zetasizer nanoseries (Nano-ZS90).
- A Raman spectrometer (with a 1064 nm Nd: YAG laser and liquid nitrogen cooled germanium detector) Bruker Vertex 70-Ram II was used to collect Raman spectral data.

- Cyclic voltammetry (CV) (potential window of -1 to 1 V vs Ag/AgCl for ferricyanide, sodium hydroxide and -0.4 to 0.6 V vs Ag/AgCl for hydrazine) were performed using Autolab potentiostat PGSTAT 302 electrochemical workstation (driven by GPES software version 4.9).
- Electrochemical impedance spectroscopy (EIS) studies were performed at 1×10^5 Hz to 0.1 Hz frequency with the applied potential of 0.24 V using an Autolab Potentiostat PGSTAT30 equipped with Nova software version 2.1. A non-linear least squares (NLLS) method based on the EQUIVCRT programme was used for automatic fitting of the obtained EIS data.
- Chronocoulometry in ferricyanide was performed on a Bioanalytical Systems 100W Electrochemical Analyzer.

2.3 Synthesis

2.3.1 Synthesis of Complex 1, Scheme 3.1

4-(Benzo[*d*]thiazol-2-ylthio) benzene-1,2-dinitrile (**i**) was synthesized according to literature **[71]**. **Complex 1** was synthesized as follows: phthalonitrile (**i)** (0.2g, 0.68 mmol) and cobalt chloride (0.02 g, 0.17 mmol) were dissolved in 1-pentanol (5 mL), followed by addition of DBU (0.3 mL). The reaction mixture was left to reflux at 200 °C for 18 h under nitrogen atmosphere. The product was then precipitated with methanol and subjected to silica gel column chromatography using THF to isolate the required product (**complex 1**).

Yield: (0.15 g) 18 %; IR (KBr, *v*, cm^{-1}): 3055-2924 (Ar-C-H), 2231(C-N), 1600 (C=N, 1411 Ar-C=C), 750 (C-S). UV/Vis (THF) λ_{max} (nm) (log ε): 667 (4.87), 606 (4.37), 331

(4.82). Elemental analysis Calc. for $C_{60}H_{28}N_{12}S_8.5H_2O$: C = 54.50, N =12.72; found: C =53.16, N = 11.44; MALDI TOF MS *m/z*: Calcd: 1232.96; Found: $[M]^+$= 1231.56.

2.3.2 Synthesis of Complex 2, Scheme 3.2

Mercaptopropionic acid phthalonitrile **(ii)** was synthesized as reported in literature **[72]**. **Complex 2** was synthesized as follows: phthalonitrile (**ii**) (0.08 g, 0.21 mmol), phthalonitrile (**i**) (0.3 g, 1.02 mmol) and cobalt chloride (0.13 g, 1.02 mmol) were dissolved in 1-pentanol (5 mL), followed by addition of 1,8-diazabicylo [5.4.0]-undec-7-ene (DBU) (0.3 mL). The reaction mixture was refluxed at 160 ℃ for 18 h under nitrogen atmosphere. The product was then precipitated with methanol and subjected to silica gel column chromatography and eluted with tetrahydrofuran (THF)/methanol (9:1), to isolate the required product.

Yield: (0.1g) 25 %; IR (KBr, *v*, cm^{-1}): 3500-3100 (-OH), 3055-2924 (Ar-C-H), 1711 (C=O, 1556 (C=N, 1405 Ar-C=C), 1325 (C-N), 744 and 728 (C-S). UV/Vis (DMF) λ_{max} (nm) (log ε): 670 (4.61), 616 (4.11), 337 (4.51). Elemental analysis Calc. for $C_{56}H_{29}CoN_{11}O_2S_7$: C = 57.42, N = 13.15. Found: C = 56.47, N = 12.22. MALDI TOF MS *m/z*: Calcd: 1169.99; Found: $[M\text{-}OH]^+$= 1152.58 m/z.

2.3.3 π-π stacking of complexes 1 and 2 onto DNDs, Scheme 3.3

The π-π stacking was done following literature **[73]**. Briefly, DNDs (5 mg) were dissolved in dimethylformamide (DMF, 3 mL) followed by the addition of **1** or **2** (8 mg in 3 mL DMSO). The mixture was sonicated for 4 h and left stirring at room temperature for 48 h. Thereafter, the mixture was precipitated with ethanol and centrifuged at 3500 rpm for 10 min. The resulting precipitated was then left to dry in the fume hood, to form **1**-DNDs(ππ) and **2**-DNDs(ππ).

2.3.4 Covalent linkage of complex 2 to DNDs, Scheme 3.4

The formation of **2**@DNDs conjugate was achieved by activating the carboxylic group in mercaptopropionic acid moiety as follows: dicyclohexylcarbodiimide (DCC, 5.3 mg, 0.0257 mmol) and **complex 2** (12 mg, 0.011 mmol) were dissolved in 3 mL of DMF and left to stir at ambient temperature for 48h. After this time, a solution of DNDs (10 mg in 3 mL DMF) was added and the resulting mixture allowed to stir for another 48 h. The product was obtained by precipitation using ethanol and centrifuged at 3000 rpm for 10 min and is represented as **2**@DNDs.

2.4 Electrode modification

The glassy carbon electrode (GCE) was used as a working electrode, platinum wire as a counter electrode and silver|silver chloride (3 M KCl) as the reference electrode. Firstly, the GCE was polished on a polishing pad using alumina and washed with Millipore water. The modification was carried out using the drop-and-dry method as follows: 5 µL (1 mg/mL) in DMF each of **complex 1**, **complex 2**, DNDs, **1**-DNDs($\pi\pi$), **2**-DNDs($\pi\pi$) and **2**@DNDs were dropped on the GCE surface and dried for 2h at 60 °C, to give GCE/**1**, GCE/**2**, GCE/DNDs, GCE/**1**-DNDs($\pi\pi$), GCE/**2**-DNDs($\pi\pi$) and GCE/**2**@DNDs. In addition, the GCE was modified by sequential addition of the **complex 1**, **complex 2** and DNDs onto the GCE, represented as GCE/DNDs-**1**(seq), GCE/DNDs-**2**(seq) (when DNDs are placed first onto the electrode) and GCE/**1**-DNDs(seq), GCE/**2**-DNDs(seq) (when CoPc is placed first) where seq represents sequential. The solutions used for electrochemical experiments were deaerated by argon gas and the cell kept under argon atmosphere throughout the experiments.

PUBLICATIONS

The results discussed in chapters 3-5 are from the peer-reviewed publications listed below.

- L. Ncwane, L. S. Mpeta, and T. Nyokong, Electrocatalytic activity of benzothiazole substituted cobalt phthalocyanine in the presence of detonation nanodiamonds. *Diam. Relat. Mater.*, *129*, (2022) 109319.
- L. Ncwane, L. S. Mpeta, T. Nyokong, Effect of detonation nanodiamonds on the electrocatalytic behaviour of asymmetrically substituted cobalt phthalocyanine, (2022) **(Under review).**

3 CHARACTERISATION

This chapter looks into synthesis and characterisation of complexes 1, 2, 1-DNDs(ππ), 2-DNDs(ππ), 2@DNDs and DNDs alone.

3.1 Characterisation of the MPcs

The synthesis of complexes **1** and **2** was carried out by statistical condensation of the phthalonitriles, **Schemes 3.1** and **3.2**. Synthesized MPcs were characterized using different techniques to confirm their formation. The characterisation techniques employed in this work include mass and UV-visible spectroscopies, elemental analysis as well as Fourier-transform infrared spectroscopy (FT-IR). In this work nuclear magnetic resonance spectroscopy was not utilized due to the paramagnetic nature of the central metal Co^{2+} in both complexes. The elemental analysis values obtained for complex **2** are in agreement with the calculated, however for complex **1** the values are in agreement with observations that some Pcs are isolated as hydrates **[74]**.

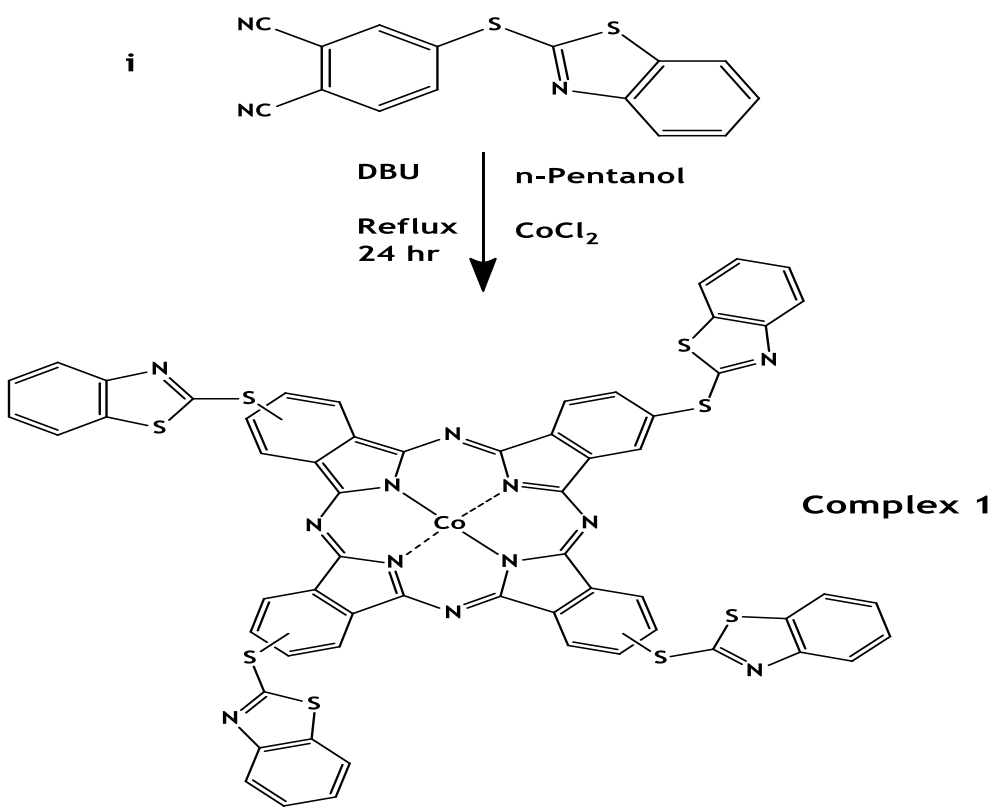

Scheme 3.1: Synthesis of complex **1**

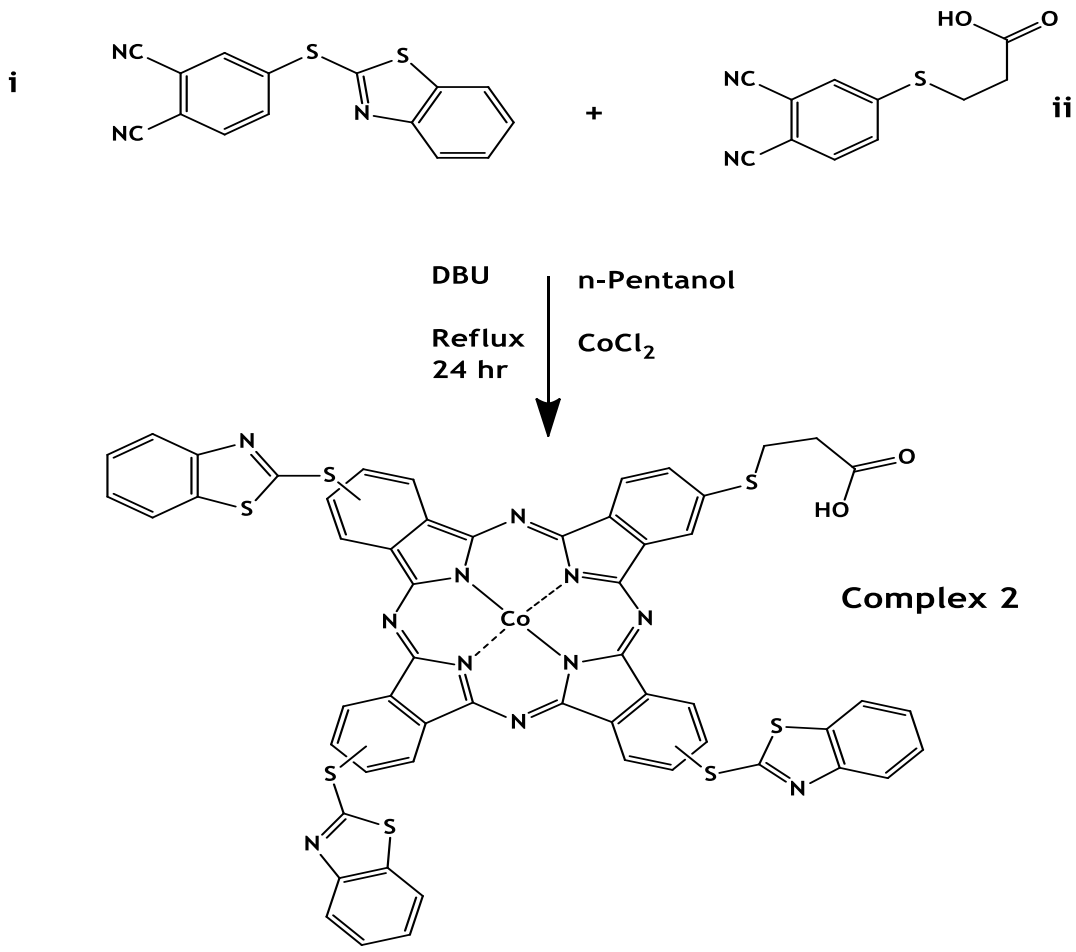

Scheme 3.2: Synthesis of complex **2**

The UV-visible spectra of the synthesized phthalocyanines are shown in (**Fig. 3.1**). **Figure. 3.1**, shows broad Q bands at 667 nm and 670 nm for complexes **1** and **2** respectively, typical of cobalt phthalocyanines **[75]**, **Table 3.1**. In addition, B bands were observed for both complexes at 331 nm for **1** and 337 nm for **2**. In comparison to unsubstituted MPc's Q bands (660 nm in THF), the synthesized complexes had red-shifts on the Q band, **Table 3.1 [76]**. The red-shits of the Q bands are due to the substituents employed in this work. The Pc ring substituents employed in this work contain sulphur, which are known to possess large electron-donating abilities, hence the red-shifts of the Q band **[77]**.

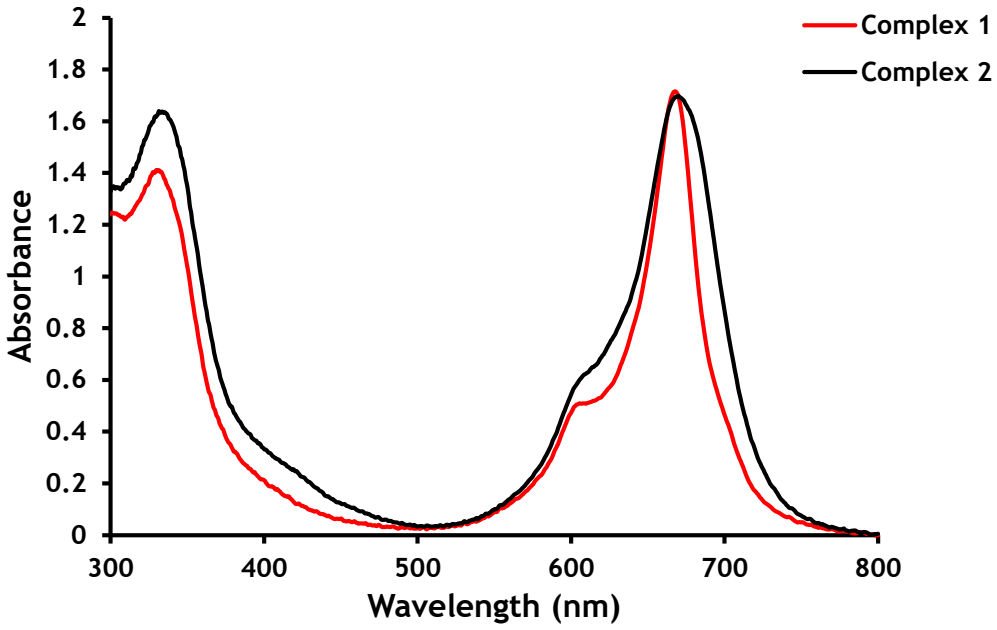

Figure 3.1: UV-visible spectra for complex **1** and **2** (14 μM) in THF.

Table 3.1: Shows parameters of the synthesized MPcs and conjugates in THF.

Complex/Conjugate/ nanomaterial	THF Q band Uv/vis (nm)	Dynamic light scattering (DLS) size (nm)
1	667	-
2	670	-
DNDs	-	3.1
1-DNDs(ππ)	669	9.7
2-DNDs(ππ)	675	18
2@DNDs	680	22

A further investigation into formation of the desired product was confirmed by mass spectra. The obtained mass form complex **1** was 1231.56 m/z, **Fig A1 (Appendix)**, whereas for complex **2** it was 1152.58 m/z, **Fig A2 (Appendix)**. The mass obtained for complex **2** was a result of OH fragmentation from the mercaptopropionic acid substituent.

Figure 3.2 shows the FT-IR spectra of the synthesized complexes **1** and **2**. The formation of phthalocyanines is confirmed by the disappearance of the nitrile peak near 2200 cm^{-1}. The peak is from phthalonitriles employed. For complex **2** FT-IR spectrum shows hydroxyl (OH) and carbonyl (C=O) peaks at 3500-3100 cm^{-1} and 1711 cm^{-1} respectively, which could be from the carboxylic acid moiety present in **2,** however these peaks were not observed for **1**, since it is a benzothiazole tetra MPc. Furthermore, C-S peaks were observed for all the compounds between 700-600 cm^{-1}.

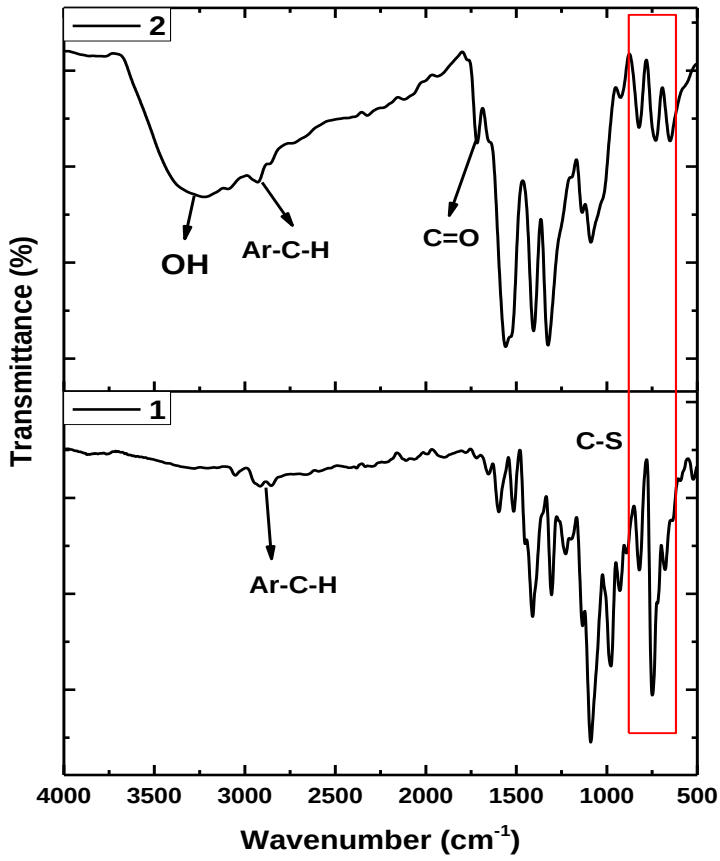

Figure 3.2: FT-IR spectra of complex **1** and **2**.

3.2 Characterisation of MPc-DNDs composites

The presence of π electrons in both the CoPcs (**1** and **2**) and DNDs allows for π-π stacking of the two, forming **1**-DNDs(ππ) and **2**-DNDs(ππ), **Scheme 3.3**. The presence of COOH on the CoPc and NH_2 on DNDs allowed for the two to be linked through a covalent bond (an amide bond), forming **2**@DNDs, **Scheme 3.4**. The characterisation of **1**-DNDs(ππ), **2**-DNDs(ππ) and **2**@DNDs was done using dynamic light scattering (DLS), transmission electron microscopy (TEM), UV-visible, Raman and FT-IR spectrometries.

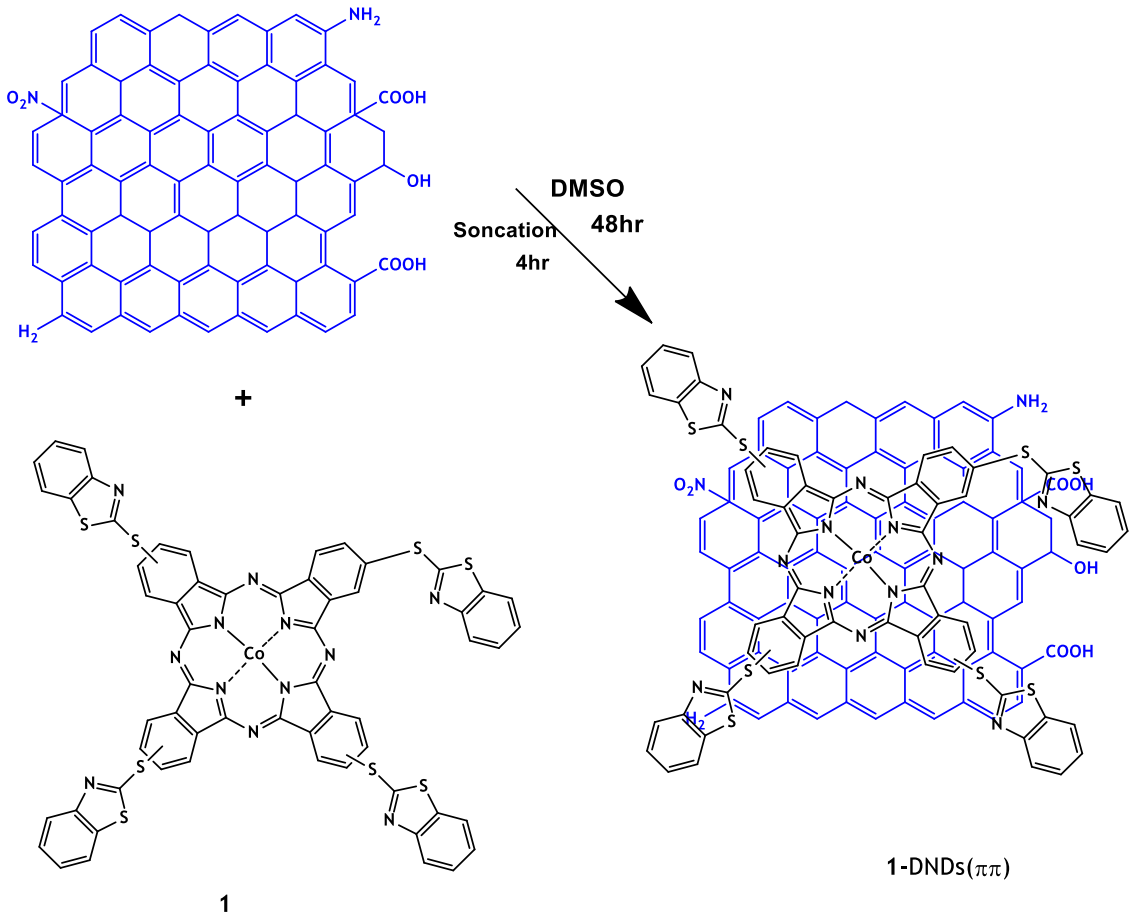

Scheme 3.3: Illustration of π-π stacking of complex **1** onto DNDs (**1**-DNDs(ππ)) as an example.

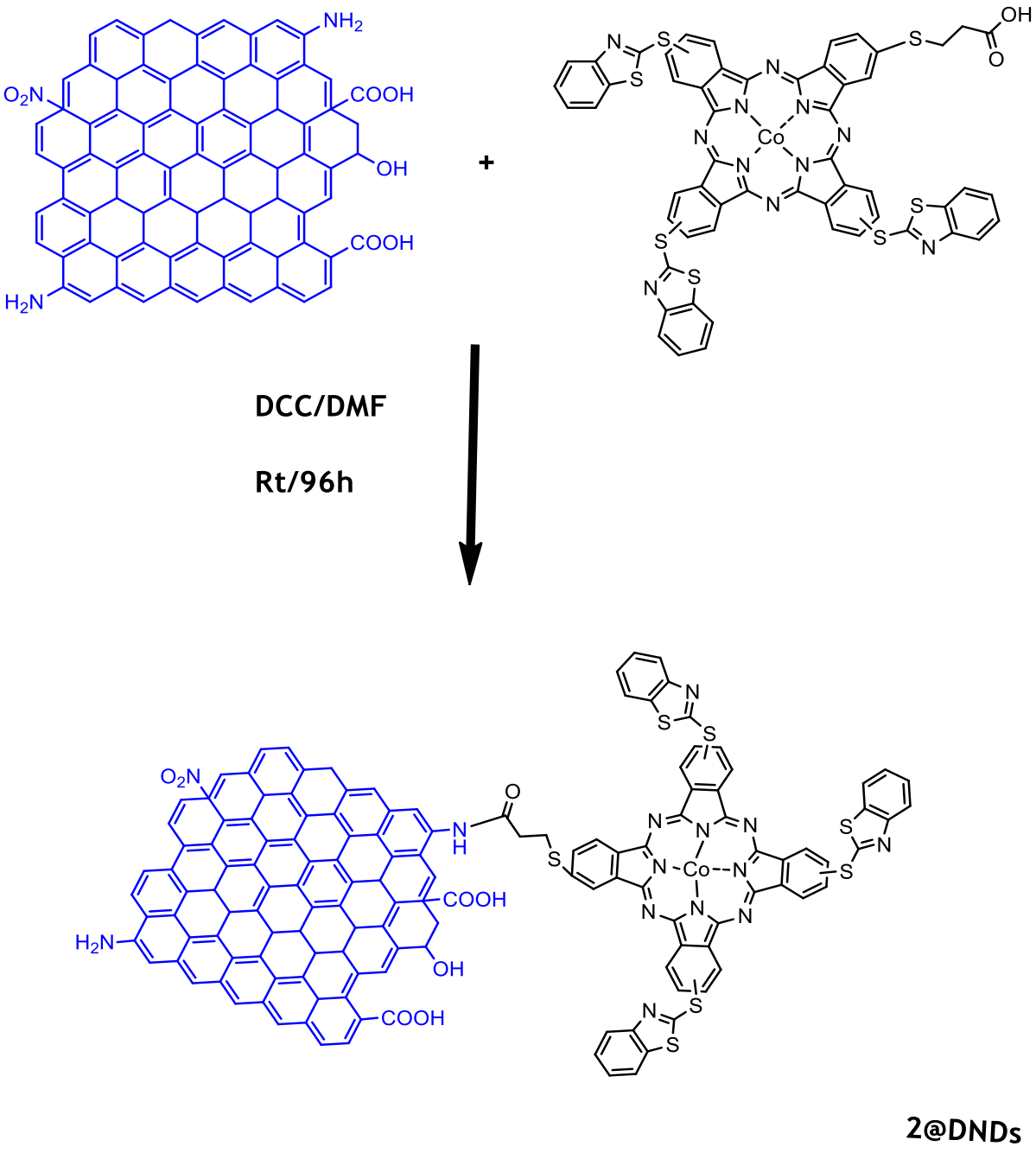

Scheme 3.4: Illustration of covalent linkage of complex **2** to detonation nanodiamonds (**2**@DNDs).

3.2.1 UV-visible spectra

Herein conjugating DNDs to MPcs is of interest, however to prove formation of the conjugates, characterisation using different techniques is important. Uv-visible spectra (**Fig.3.3**) is employed in this section. Detonation nanodiamonds do not show any absorption peak as proven in literature **[41,47]** and as shown in **Fig.3.3**. **Table 3.1** shows that upon conjugation there were Q band red shifts for all the conjugates. The red shifts are due to molecular flattening of the porphyrin **[78]**. The increase in intensity below 400 nm is due to the absorption by DNDs. For ππ stacked materials, the Q bands were broad an indication of aggregation **[47]**. The observations are an indication of successful conjugation.

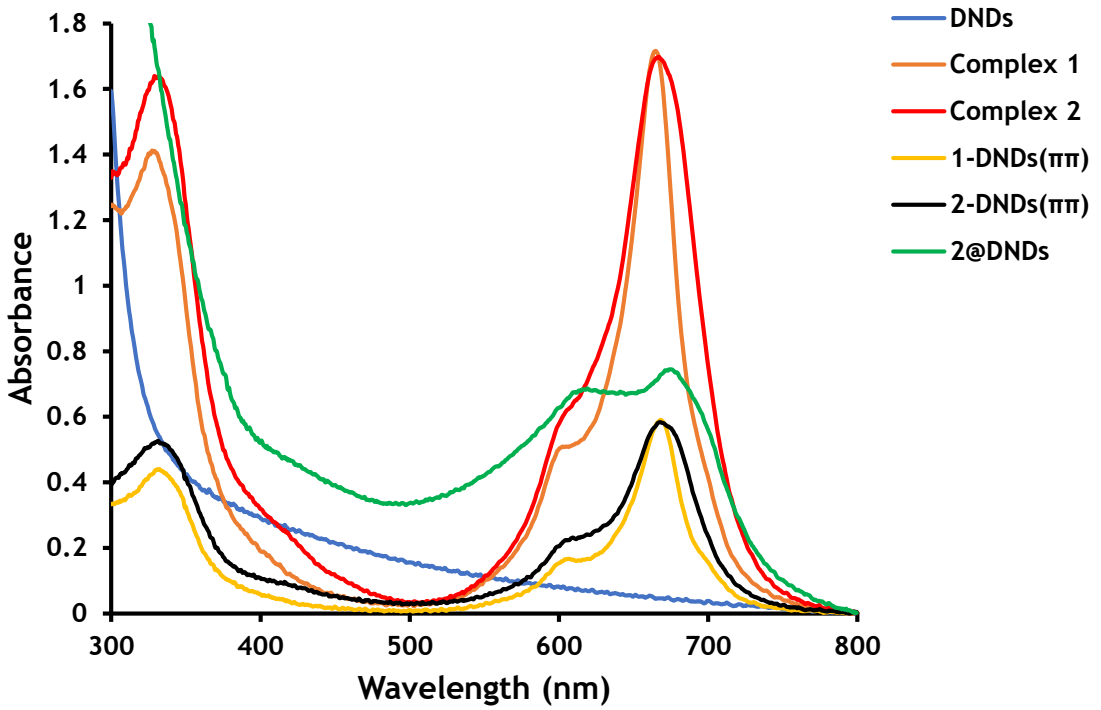

Figure 3.3: UV-visible spectra for DNDs, **1**-DNDs(ππ), **2**-DNDs(ππ) and **2**@DNDs.

3.2.2 FT-IR

The FT-IR spectra of DNDs and the conjugates (**2**-DNDs(ππ) and **2**@DNDs) are shown in **Fig. 3.4**. Of interest in this case, are stretching/vibrational frequencies associated with the amide group. The shifting of the C=O stretching at 1711 cm^{-1} of complex **2** (**Fig. 3.2**) to a sharp peak at 1656 cm^{-1} (**Fig. 3.4**) is a characteristic of amide group formation for **2**@DNDs.

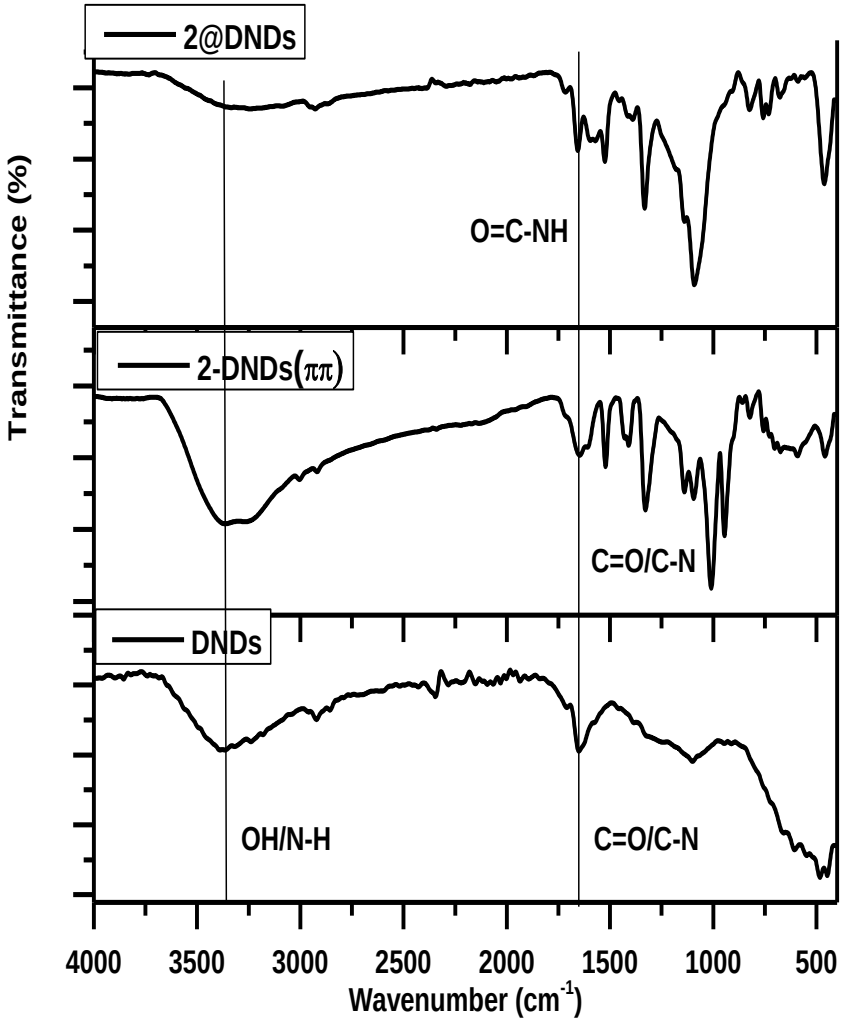

Figure 3.4: FTIR spectra of DNDs, **2**-DNDs(ππ) and **2**@DNDs.

3.2.3 TEM and DLS

The TEM images shown in **Fig. 3.5**, illustrates that DNDs are spherical in shape and there is aggregation in conjugates (**1**-DNDs(ππ) (b) **2**@DNDs (c) and **2**-DNDs(ππ) (d)). The images did not clearly provide the size, hence DLS **Fig. 3.6** was employed.

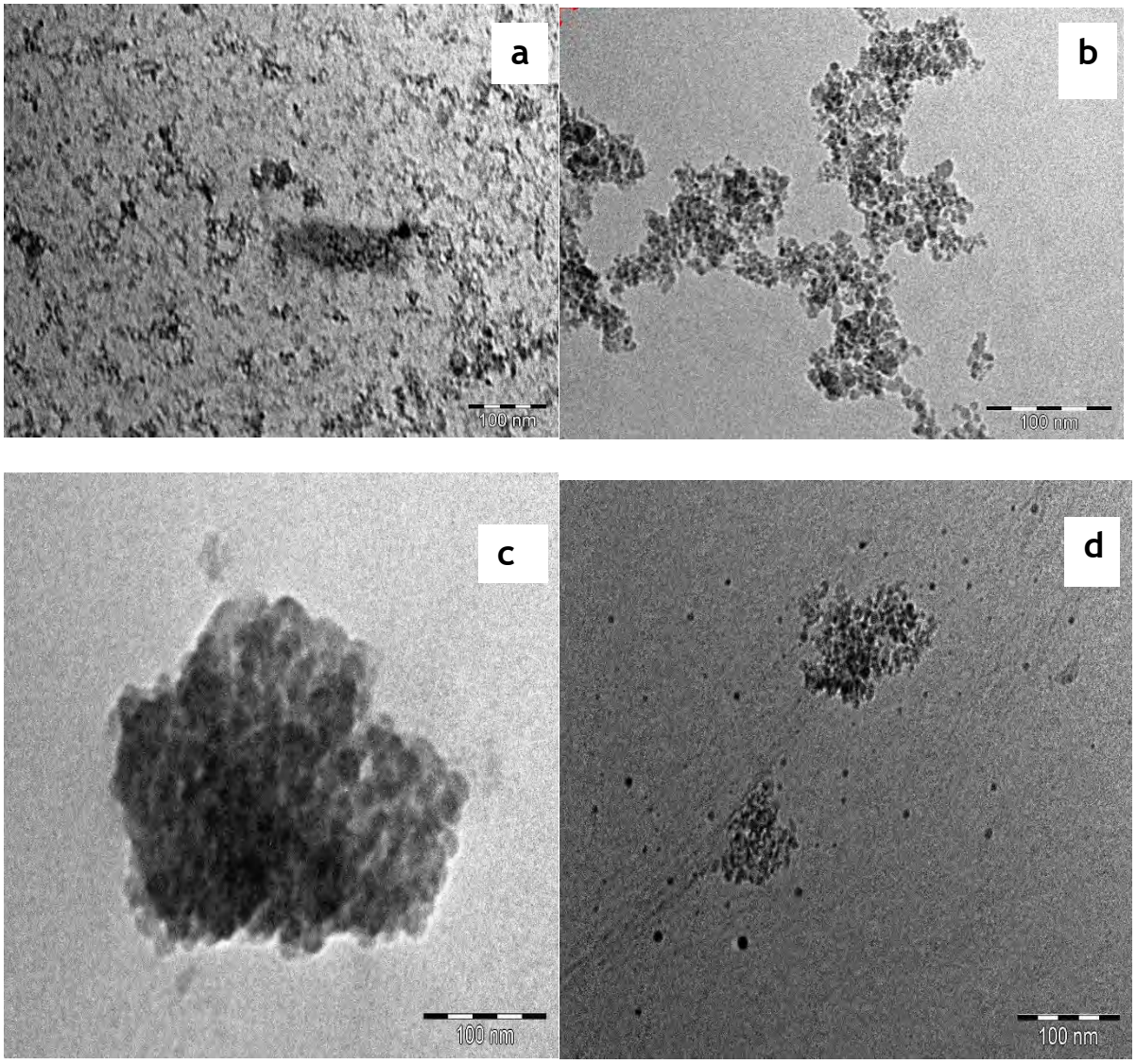

Figure 3.5: TEM images of (a) DNDs, (b) **1**-DNDs(ππ), (c) **2**-DNDs(ππ) and (d) **2**@DNDs.

DLS plots **Fig 3.6** show the size of the DNDs, **1**-DNDs(ππ), **2**-DNDs(ππ) and **2**@DNDs. The data obtained from DLS reveals a noticeable increase in the size upon conjugation of DNDs and MPcs, the sizes are 3.1 nm, 9.7 nm, 18 nm, 22 nm for DNDs, **1**-DNDs(ππ), **2**-DNDs(ππ) and **2**@DNDs, respectively (**Table 3.1**). The size increase observed from DLS may be due to aggregation, which is an indication of the interactions between the MPcs and the adjacent nanoparticles via π-π stacking. Particles of this nature (DNDs and Pcs) are susceptible to aggregation due to high electron density, hence an increase in size is observed for the conjugates. In addition, the aggregation is a result of interactions between the MPc and the adjacent nanomaterials via π-π stacking, since Pcs are known for their π-π stacking **[79]**. There larger diameters for **2**-DNDs(ππ) and **2**@DNDs indicate that there were larger aggregates **[80]**, however the bulkier nature of complex **1** may have prevented aggregation in **1**-DNDs(ππ).

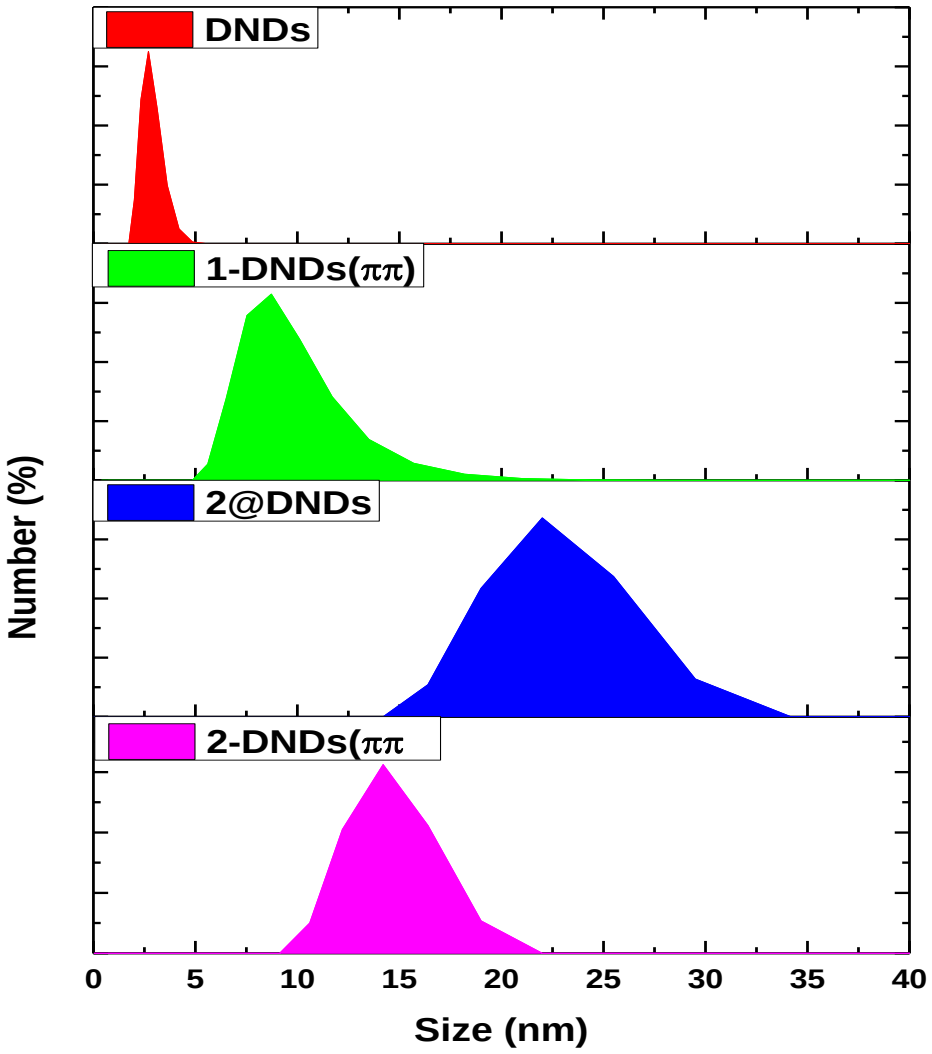

Figure 3.6: Dynamic Light Scattering plots for DNDs, **1**-DNDs(ππ), **2**-DNDs(ππ) and **2**@DNDs in DMSO.

3.2.4 Raman spectroscopy

Raman spectrometry **Fig. 3.7** was utilized to determine the quality of the DNDs and the conjugates (**1**-DNDs(ππ), **2**-DNDs(ππ) and **2**@DNDs). The Raman spectra (**Fig. 3.7**) shows the disorder (D) sp^3 defects and graphitic (G) sp^2 peaks for all materials empolyed in this work. The D and G peak positions are shown in **Table 3.2**. The data in **Table 3.2** reveals that the D bands for **1**-DNDs(ππ) and **2**-DNDs(ππ) shifted to

lower wavenumbers, whereas covalently linked conjugate **2**@DNDs to higher wavenumber of 1210 cm^{-1} when compared to DNDs alone.

Table 3.2 shows that all the conjugates had low wavenumbers for graphitic (G) sp^2 peaks in comparison with DNDs alone. The shifts in ππ stacked materials is attributed to strong π interactions between MPcs and zero-dimensional carbon allotropes and other factors such as strain of the carbon nanomaterials, diameter and nature **[81,82]**. In addition, the excitation wavelength and crystalline size of materials also alter the position and width of Raman bands **[82]**.

Table 3.2: Shows the disorder (D) sp^3, graphitic (G) sp^2 peaks and I_D/I_G ratios for DNDs and the conjugates.

Material	**(D) sp^3 peaks**	**G sp^2 peaks**	**I_D/I_G ratios**
DNDs	1115 cm^{-1}	1430 cm^{-1}	0.19
1-DNDs(ππ)	1045 cm^{-1}	1426 cm^{-1}	0.21
2-DNDs(ππ)	1050 cm^{-1}	1418 cm^{-1}	0.33
2@DNDs	1210 cm^{-1}	1365 cm^{-1}	0.79

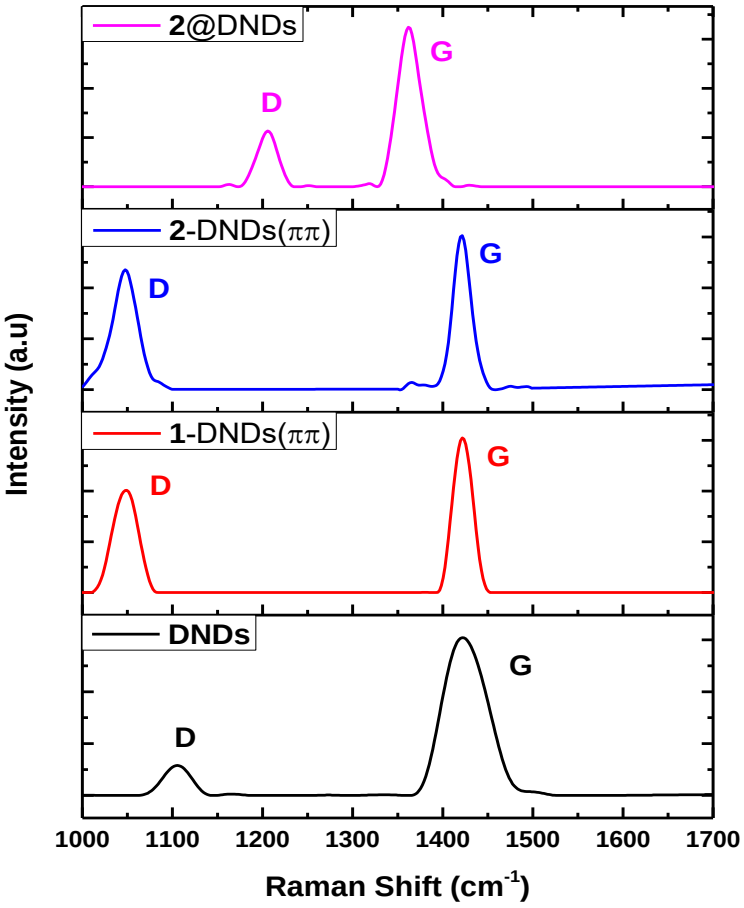

Figure 3.7: Raman spectra of DNDs, **1**-DNDs(ππ), **2**-DNDs(ππ), **2**@DNDs

The extent of interaction between DNDs and MPcs employed in this work were determined by the ratio of D to G bands: I_D/I_G (sp^3/sp^2). The I_D/I_G ratios give information about the structural changes on the conjugates. The obtained values from I_D/I_G for DNDs were 0.19, 0.21 for **1**-DNDs(ππ), 0.33 for **2**-DNDs(ππ) and 0.79 for **2**@DNDs as shown in **Table 3.2**. There is only a small increase for ππ conjugates showing that π-π stacking of Pcs and DNDs does not significantly alter the sp^2 lattice of the DNDs. Lower I_D/I_G ratio values indicate lower disorders **[83]**. In addition, the

high I_D/I_G ratio for **2**@DNDs indicates that covalent linkage altered the sp^2 of lattice of the materials significantly.

3.3 Summary of the chapter

The spectroscopic characterisation of the synthesized materials confirmed successful synthesis. FT-IR, mass spectra, elemental analysis and UV-visible spectra were successfully employed for complexes **1** and **2** characterisation. Confirmation of the formation of conjugates (**1**-DNDs(ππ), **2**-DNDs(ππ) and **2**@DNDs) was conducted using FT-IR, TEM and DLS for morphology and size, Raman and UV-visible spectroscopies.

4 CHARACTERISATION OF THE MODIFIED ELECTRODES

This chapter discusses characterisation of the modified electrodes in ferricyanide for electron transfer and sodium hydroxide.

4.1 Studies in ferricyanide

4.1.1 Cyclic voltammetry

Ferricyanide is a known redox probe for the characterisation of GCEs. The choice is motivated by high reversibility and stability of this probe **[84]**. Cyclic voltammetry (**Figure 4.1**) was employed to probe electrochemical properties such as the charge transfer ability of the modified electrodes in 1 mM $[Fe(CN)_6]^{3-/4-}$ in 0.1 M KCl solution. The properties were determined by anodic to cathodic peak potential separation. Anodic to cathodic peak potential differences (ΔE_p) are shown in (**Table 4.1**), with the bare electrode showing the lowest ΔE_p. The GCE/**1**, GCE/**2** and GCE/DNDs-**2**(seq) probes had the highest ΔE_p values, an indication of a blocked surface. Lower ΔE_p values are an indication of a good electron transfer abilities. This observation reveals that the bare electrode has a better charge transfer than all the modified electrodes. However, the lowest ΔE_p value is not only synonymous with desirable electron-transporting abilities but is also often associated with a clean electrode surface. **Table 4.1** shows that incorporating DNDs to MPcs improves electron transfer abilities of the MPc. However, this provides no information about the charge transfer in the presence of hydrazine. The increasing order of ΔE_p from **Table 4.1**; Bare GCE < GCE/DNDs < GCE/**2**-DNDs(seq) < GCE/DNDs-**1**(seq) < GCE/**2**-DNDs(ππ) < GCE/**2**@DNDs < GCE/**1**-DNDs(seq) < GCE/**1**-DNDs(ππ) < GCE/**1** < GCE/DNDs-**2**(seq) < GCE/**2**. The trend shows that sequentially modified GCE/DNDs-**2**(seq), had the highest ΔE_p than other electrodes in the presence of DNDs. In terms of electron transfer abilities of the sequentially modified electrodes, when the MPc is on top GCE/DNDs-**1**(seq) had better ΔE_p compared to GCE/**1**-DNDs(seq). However, for complex **2** electrodes GCE/**2**-DNDs(seq) performed better.

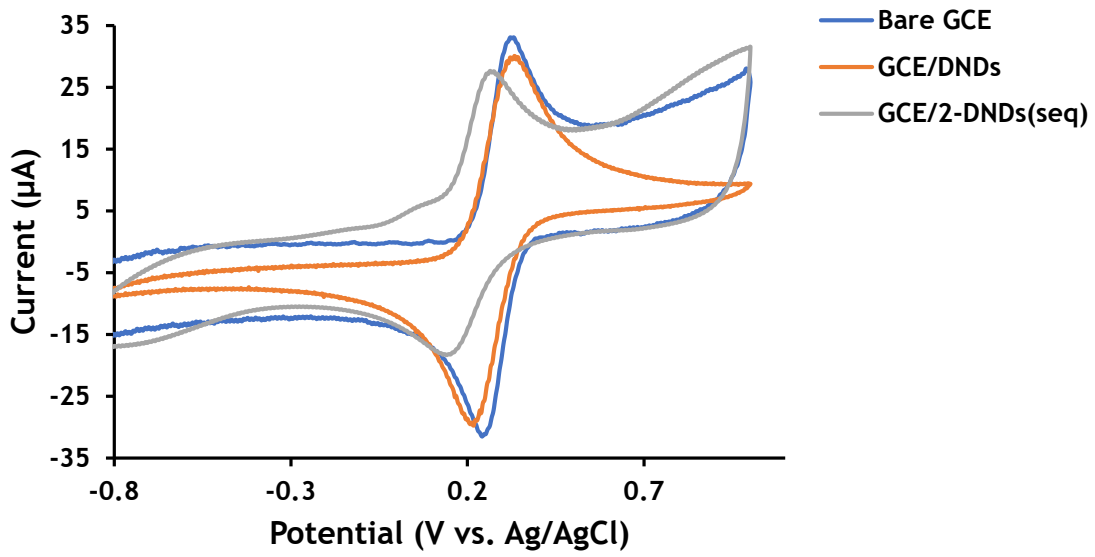
Bare GCE
GCE/DNDs
GCE/2-DNDs(seq)
Current (µA)
35
25
15
5
-5
-15
-25
-35
-0.8
-0.3
0.2
0.7
Potential (V vs. Ag/AgCl)

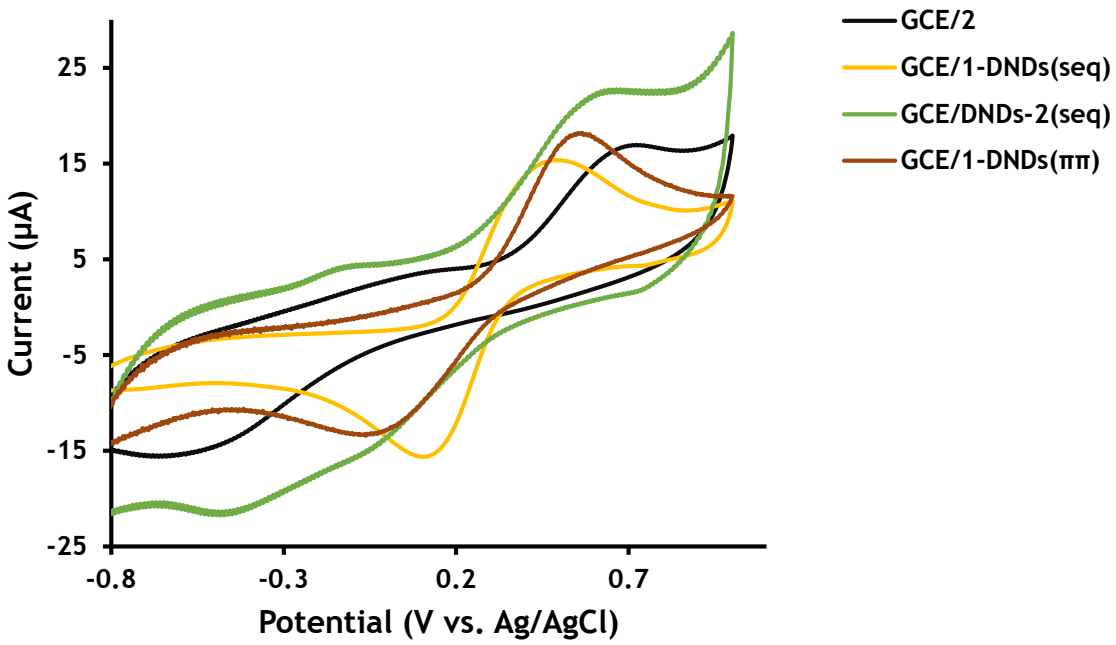
GCE/2
GCE/1-DNDs(seq)
GCE/DNDs-2(seq)
GCE/1-DNDs(ππ)
Current (µA)
25
15
5
-5
-15
-25
-0.8
-0.3
0.2
0.7
Potential (V vs. Ag/AgCl)

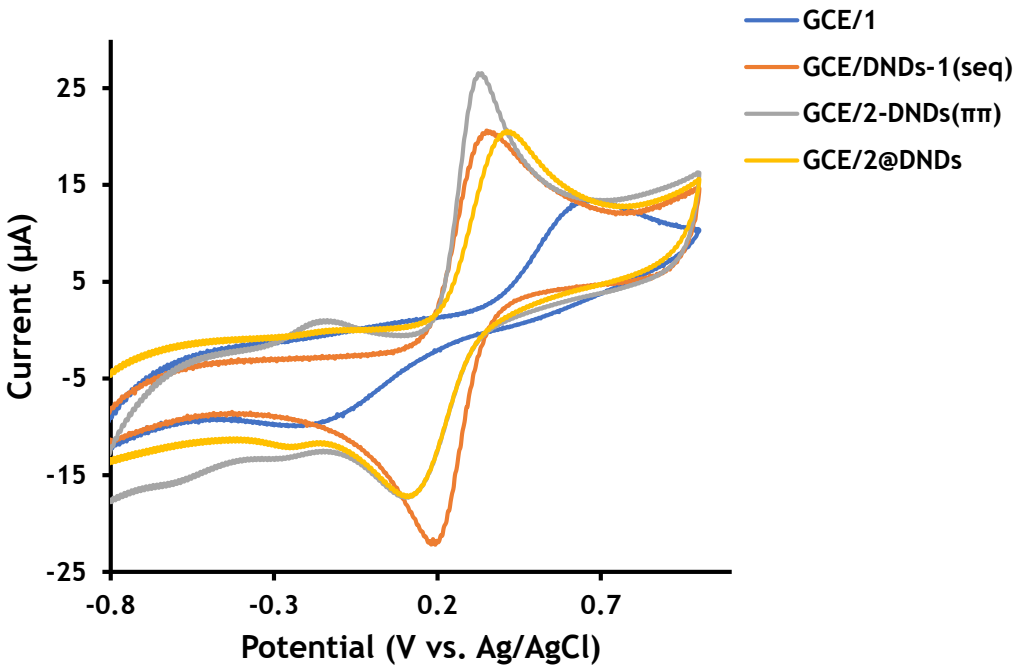

Figure 4.1: Cyclic voltammograms of the bare and modified glassy carbon electrodes in 1 mM $[Fe(CN)_6]^{3-/4-}$ in 0.1 M KCl solution at 100 mV/s scan rate.

4.1.2 Chronocoulometry

The active areas of the modified electrodes were determined using chronocoulometric experiments. **Figure 4.2**, illustrates the plots of charge versus time and charge versus square root of time which was obtained by stepping the potential from 0 V to 1 V. The plot **Fig. 4.2**, was used with integrated Cottrell equation (**Eq. 4.1**) in determining the active area and to calculate the surface coverage (**Table 4.1**) **[85]**.

$$Q = \frac{2nFAD^{1/2}C_0t^{1/2}}{\pi^{1/2}} \qquad (4.1)$$

where n= number of electrons, A = the effective surface area, C_0 = concentration of $[Fe\ (CN)_6]^{3-/4}$, F the Faraday's constant (96,485 $C.mol^{-1}$), t = time, D = diffusion coefficient 7.6×10^{-6} cm^2/s of according to literature **[86]**. The calculated effective area was employed in calculating the surface coverage under section 4.2 (**Table 4.1**).

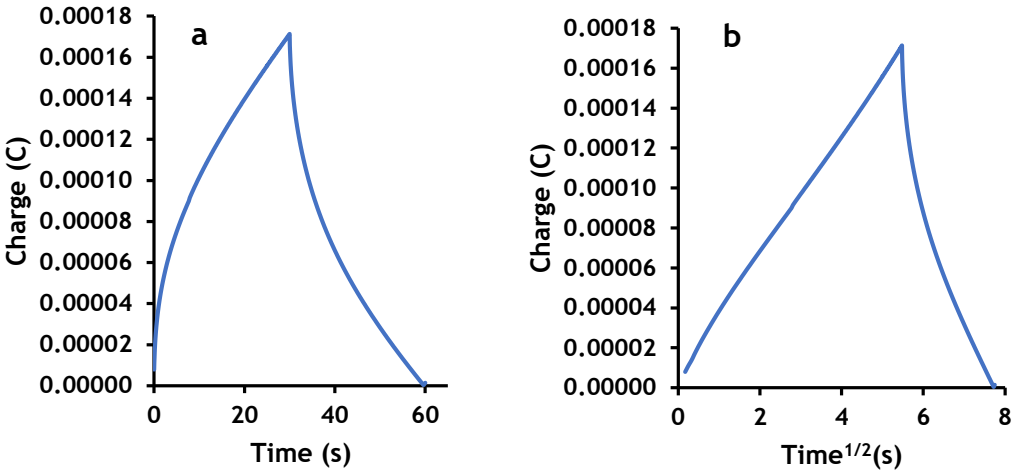

Figure 4.2: Chronocoulometric plots of GCE/CoPc@DNDs (a) charge vs. time and (b) charge vs. square root of time in 1 mM $[Fe(CN)_6]^{3-/4-}$ in 0.1 M KCl.

Table 4.1: Table showing ΔE_p, surface coverage and Rct values in ferricyanide solution.

Electrodes	Rct(kΩ)	ΔE_p (mV)	Γ (mol cm^{-2})
Bare GCE	0.035	78	-
GCE/DNDs	0.93	115	5.60×10^{-7}
GCE/**1**	74.7	822	1.63×10^{-6}
GCE/**2**	17.8	1340	8.36×10^{-7}
GCE/DNDs-**1**(seq)	6.86	156	1.01×10^{-6}
GCE/**1**-DNDs(seq)	12.2	325	1.27×10^{-6}
GCE/**1**-DNDs(ππ)	42.4	537	7.13×10^{-7}
GCE/DNDs-**2**(seq)	15.9	1021	1.88×10^{-6}
GCE/**2**-DNDs(seq)	14.9	142	7.00×10^{-7}
GCE/**2**-DNDs(ππ)	11.0	230	4.59×10^{-7}
GCE/**2**@DNDs	14.4	283	1.53×10^{-6}

4.1.3 Electrochemical impedance spectroscopy (EIS)

The charge transfer resistance was further investigated by EIS experiments. The Nyquist plots **(Fig. 4.3)** were used to obtain charge transfer resistance (R_{ct}) values using the Randles model for circuit fitting, **Fig. 4.3d**. To predict the charge-transfer abilities of the electrodes, semi-circles from the Nyquist plots are employed. A large semi-circle reveals that the material is more insulating resulting in poor charge transfer abilities, whereas a small diameter implies fast electron movement. The R_{ct} values obtained from the Nyquist plots show that bare electrode had the lowest R_{ct}

of 0.035 kΩ which is lower than for modified electrodes. A lower R_{ct} value shows that there are better charge transfer kinetics. The incorporation of the DNDs to complexes **1** and **2** improved the charge transfer abilities of the probes. **Table 4.1**, shows that GCE/DNDs-**1**(seq) had a better charge transfer ability in terms of R_{ct} than other electrodes, probably because in the former the CoPc is on top. As stated above MPcs are known to overcome the problems of slow kinetics **[55]**, hence when placed on top of DNDs, CoPc is exposed and mediates more efficiently in GCE/DNDs-**1**(seq), but it is not the case for GCE/DNDs-**2**(seq). The R_{CT} values obtained from EIS do not entirely corroborate with ΔE_p values from cyclic voltammetric experiments, with GCE/**1**, GCE/**2** and GCE/**1**-DNDs(ππ) being the worst performing in EIS.

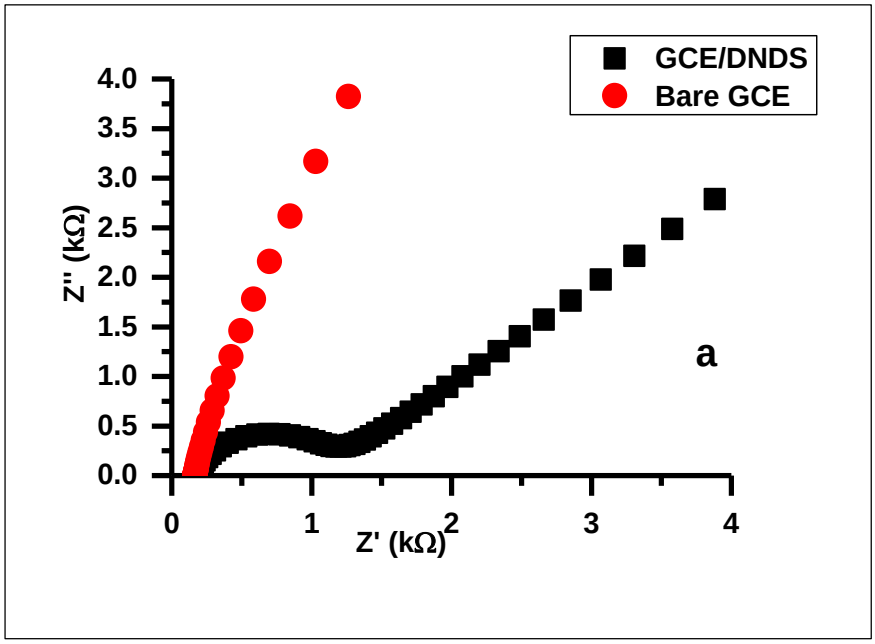

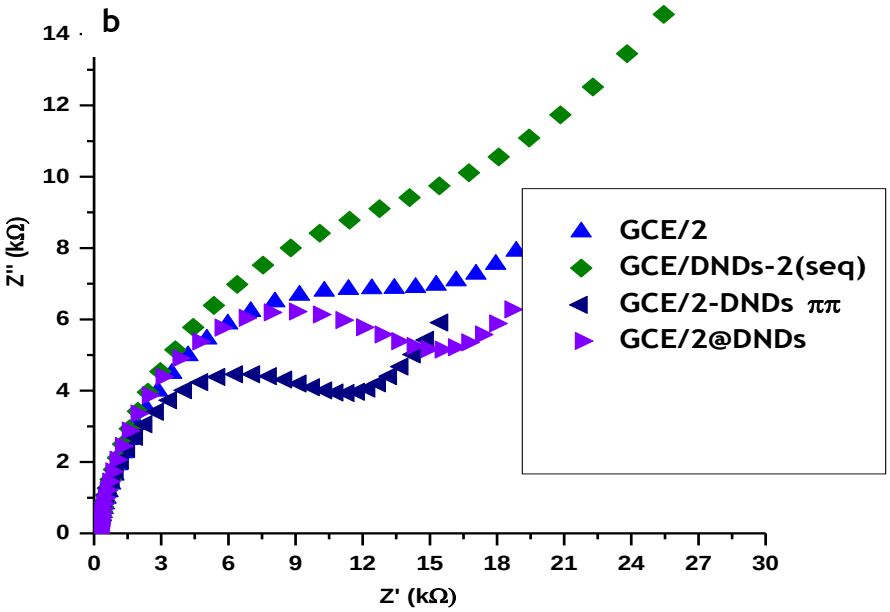
b
Z'' (kΩ)
Z' (kΩ)
GCE/2
GCE/DNDs-2(seq)
GCE/2-DNDs ππ
GCE/2@DNDs

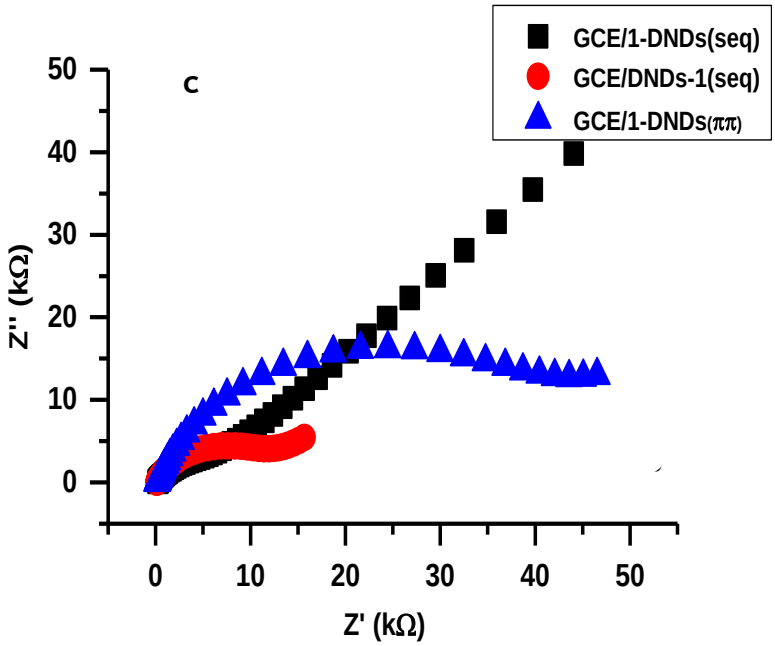
c
Z'' (kΩ)
Z' (kΩ)
GCE/1-DNDs(seq)
GCE/DNDs-1(seq)
GCE/1-DNDs(ππ)

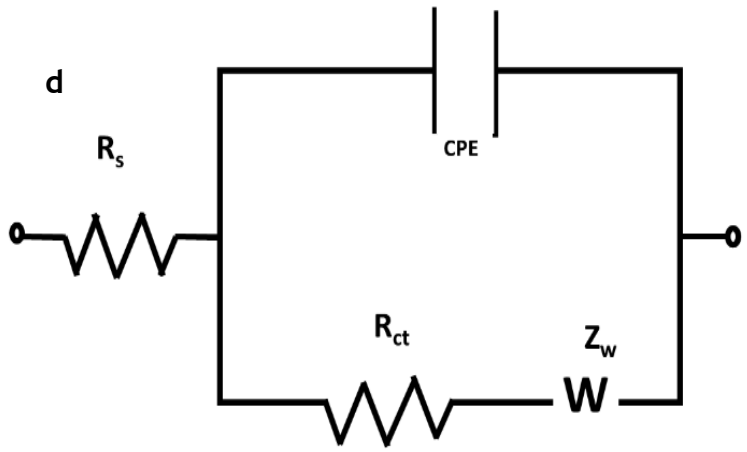

Figure 4.3: Comparative Nyquist plots in 1 mM $[Fe(CN)_6]^{3-/4-}$ of (a) bare GCE and GCE/DNDs, (b) GCE/**1**-DNDs(seq), GCE/DNDs-**1**(seq), GCE/**1**-DNDs(ππ), (c) GCE/**2**, GCE/DNDs-**2**(seq), GCE/**2**-DNDs(ππ) and GCE/**2**@DNDs, (d) Randles fitting model employed.

4.2 Cyclic voltammetry in sodium hydroxide

Cyclic voltammograms in sodium hydroxide as a supporting electrolyte were conducted to understand the electrocatalytic activities of the electrodes in the absence of an analyte. **Figure 4.4**, shows CVs of electrodes employed in this work in 0.1 M NaOH.

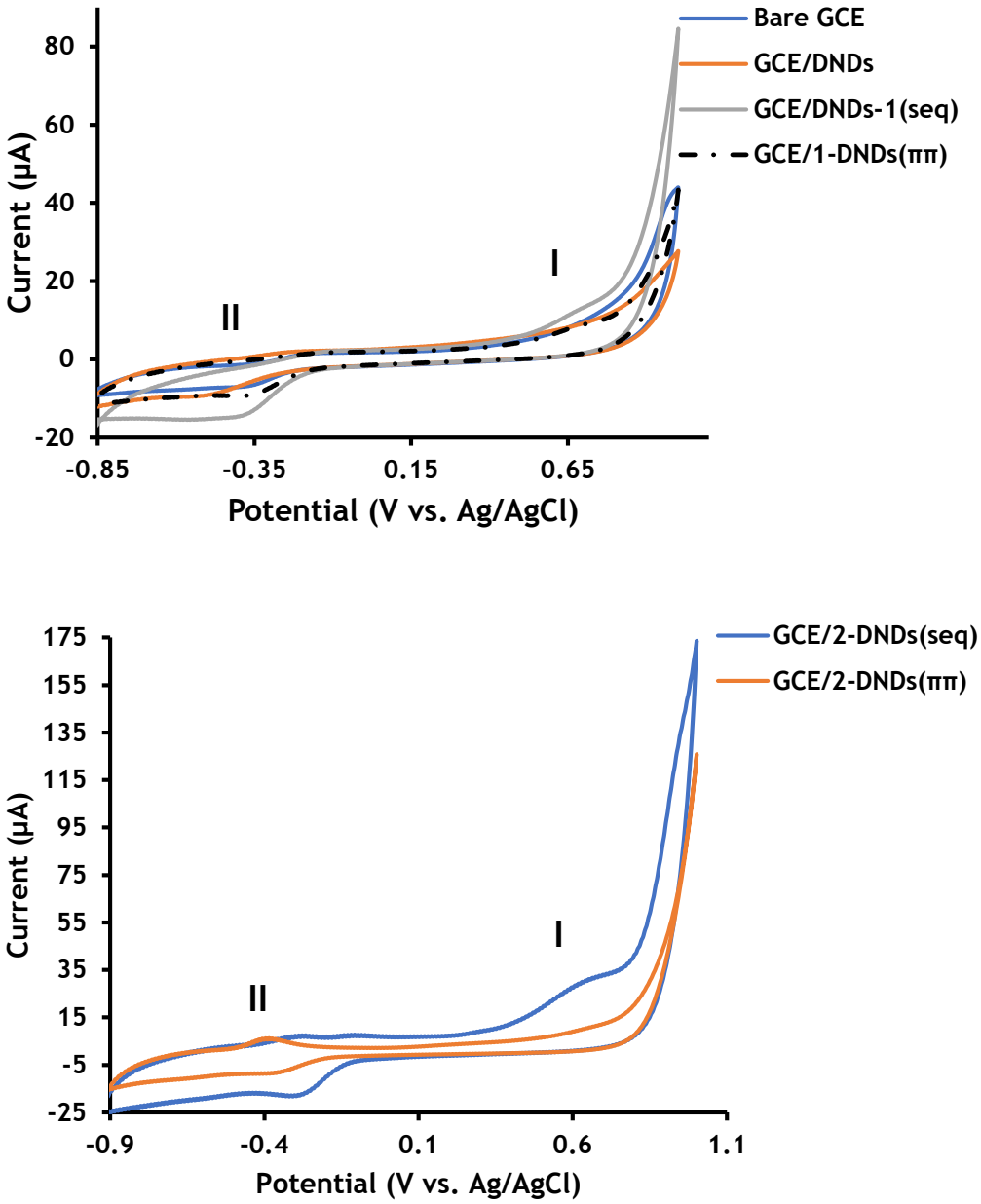

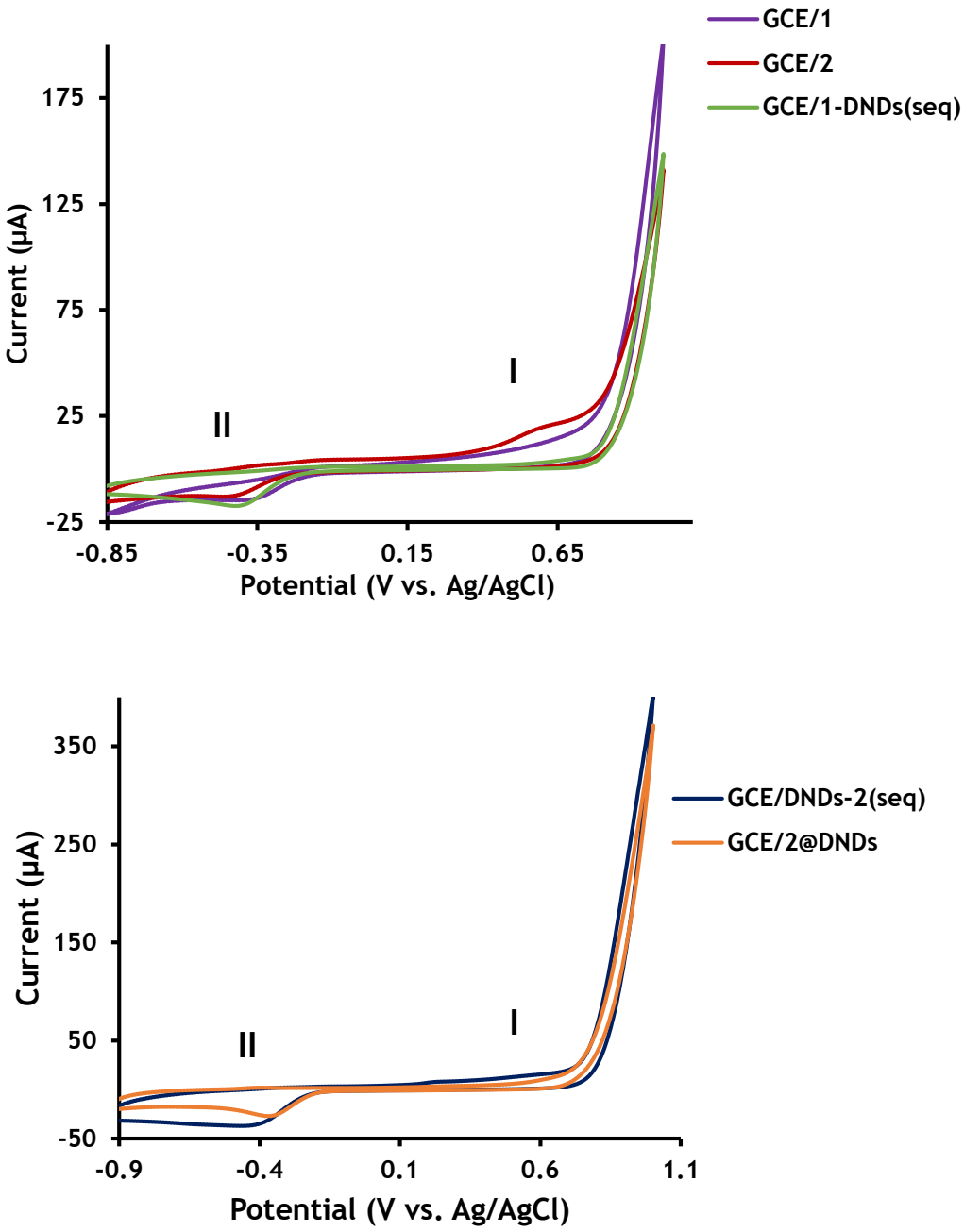

Figure 4.4: Cyclic voltammograms of the bare and modified electrodes in 0.1 M sodium hydroxide solution at 100 mV/s scan rate.

The oxidation peaks (labelled **I**) were observed for GCE/DNDs-**1**(seq), GCE/DNDs-**2**(seq) and GCE/**2** between 0.55 V and 0.65 V, are due to $Co^{III}Pc^{-2}/Co^{II}Pc^{-2}$ process in comparison with literature **[87]**. For CoPc containing electrodes, the reduction

peaks between -0.3 to - 0.6 V (labelled **II**) are attributed to Co(II)/Co(I) processes **[55, 88]**, this process mediates in the oxidation of hydrazine according to **Eqns 1.1-1.4.** Peak near a potential of -0.5 V for DNDs alone has been observed for other zero-dimensional carbon allotropes as graphene quantum dots **[89]**. DNDs possess oxygen-rich groups at the surface, which may result in rich redox chemistry.

The calculated effective area **Eqn 4.1** was used to calculate surface coverage shown in, **Table 4.1** using **equation 4.2 [90]**.

$$\Gamma = \frac{Q}{nFA} \qquad \textbf{(4.2)}$$

where Γ is the surface coverage, Q the integrated surface area of the modified electrode, n the number of electrons transferred, F the Faraday's constant (96,485 $C.mol^{-1}$) and A is the effective surface area calculated from **Eq. 4.1**. The intergrated surface area (Q) was determined from the process labelled **II** in **Fig.4.4.**

The calculated values of surface coverage are shown in **Table 4.1**. The data obtained reveals that GCE/**1**, GCE/DNDs-**2**(seq) and GCE/**2**@DNDs had the highest surface coverages than other modified probes. Pcs forming a flat monolayer on electrode's surface have a surface coverage of 1 x 10^{-10} mol/cm^2 or lower **[91]**. But in this case the obtained *Γ* values are higher and may imply the formation of multi-layered films.

4.3 Summary of the chapter

In this chapter electrochemical characterisation of the modified electrodes was presented. The CVs obtained from ferricyanide show that after modification, the electrodes had poor electron transfer abilities when compared to bare GCE. This is an indication of successful modification. Electrochemical impedance spectroscopy further proves this, since some of the Rct values corroborate with CV results studied in ferricyanide. The CVs conducted in sodium hydroxide as a supporting electrolyte were used to calculate surface coverage. Information obtained implied that modified electrodes had multi-layered films.

5 HYDRAZINE ELECTROCHEMICAL SENSING

Electrochemical determination of hydrazine is discussed in this chapter.

5.1 Cyclic voltammetry

The electrocatalytic parameters of the modified electrodes listed in **Table 5.1** were carried out in 5 mM of hydrazine in 0.1 M NaOH. **Figure 5.1** illustrates comparative cyclic voltammograms for hydrazine electrochemical detection. The important information obtained from the plots in **Fig. 5.1** and data in **Table 5.1** is as follows:

- Bare GCE and GCE/DNDs electrodes did not show any peaks for the oxidation of hydrazine.
- The GCE/**1**, GCE/**2,** GCE/DNDs-**1**(seq), GCE/**1**-DNDs(seq) and GCE/**1**-DNDs(ππ), GCE/**2**-DNDs(seq), GCE/DNDs-**2**(seq), GCE/**2**-DNDs(ππ), and GCE/**2**@DNDs showed prominent oxidation peaks, with GCE/**2**@DNDs having highest background corrected current (at 86 μA) and a negatively shifted oxidation potential (at 0.09 V, similar to GCE/DNDs-**2**(seq) at 0.08 V), **Table 5.1**. Other probes have high potentials between 0.12 - 0.32 V.
- Even though GCE/**1** and GCE/**1**-DNDs(seq) showed a relatively low oxidation potential for hydrazine, they gave low background corrected currents, when compared to the currents observed for GCE/DNDs-**1**(seq) and GCE/**1**-DNDs(ππ).
- Sequentially modified electrodes perform, better in terms of background corrected current when the MPc is on top, whereas electrodes with DNDs on top recorded lower currents. This is because CoPc is not exposed. When the CoPc is exposed it mediates more efficiently than when it is not exposed. In addition, the probes containing asymmetrical Pc (**2**) performed better highlighting the importance of low symmetry.

- Further highlighting an importance of putting MPc on top in sequentially modified electrodes, GCE/DNDs-**2**(seq) compared to GCE/**2**-DNDs(seq), GCE/DNDs-**1**(seq) compared with GCE/**1**-DNDs(seq), higher currents were reported when MPcs are on top. For complex **2**, this corresponds to higher surface coverage when the MPcs were on top (**Table 5.1**).
- Comparing GCE/**2**-DNDs(ππ) with GCE/**2**@DNDs shows that the lowest oxidation potential and highest current are observed for the latter (**Table 5.1**), showing the advantage of covalent linking. The higher current in GCE/**2**@DNDs corresponds to high surface coverage.

The observations from this data show the significant role of the DNDs, as it has been shown that nanomaterials improve the electrocatalytic activity of phthalocyanines. However, in some cases DNDs did not improve the electrocatalytic activity in terms of current (e.g GCE/**1**-DNDs(seq). Since DNDs have a conjugated π system, they donate electrons to the CoPc ring which results in the enhancement of CoPc's electrocatalytic ability towards hydrazine.

Cyclic voltammograms of the modified electrodes show double oxidation peaks towards hydrazine in some cases. The double oxidation peaks are known to result from the regeneration of the active electrocatalysit on electrode's surface, which oxidizes hydrazine **[92]**.

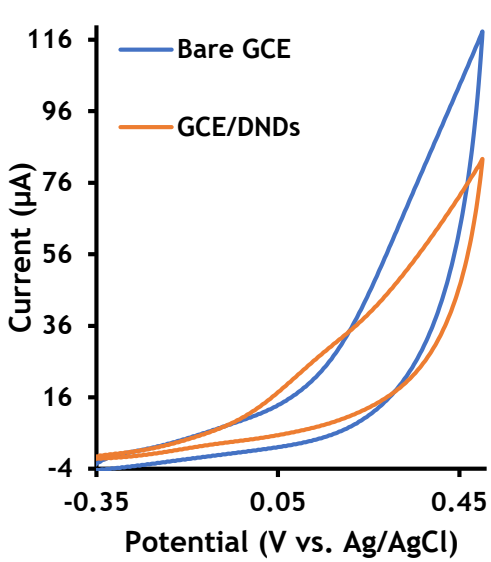
Bare GCE
GCE/DNDs
Current (μA)
116
96
76
56
36
16
-4
-0.35
0.05
0.45
Potential (V vs. Ag/AgCl)

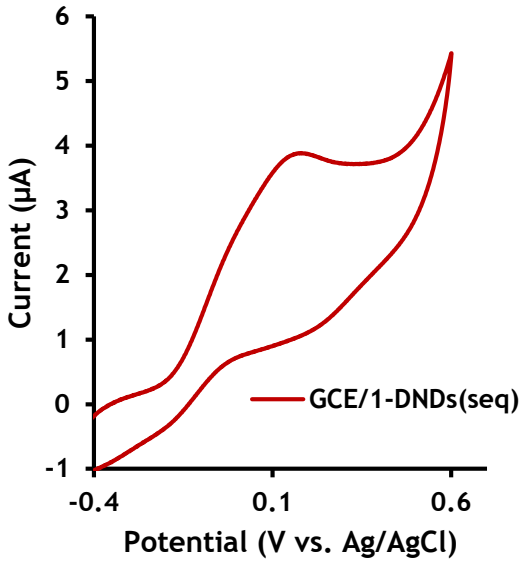
GCE/1-DNDs(seq)
Current (μA)
6
5
4
3
2
1
0
-1
-0.4
0.1
0.6
Potential (V vs. Ag/AgCl)

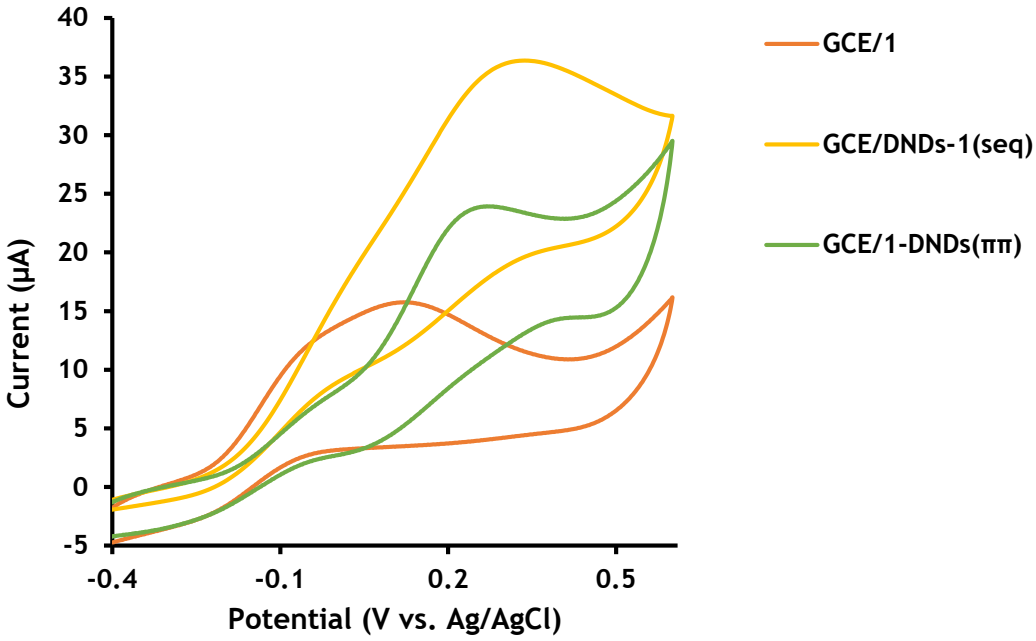
GCE/1
GCE/DNDs-1(seq)
GCE/1-DNDs(ππ)
Current (μA)
40
35
30
25
20
15
10
5
0
-5
-0.4
-0.1
0.2
0.5
Potential (V vs. Ag/AgCl)

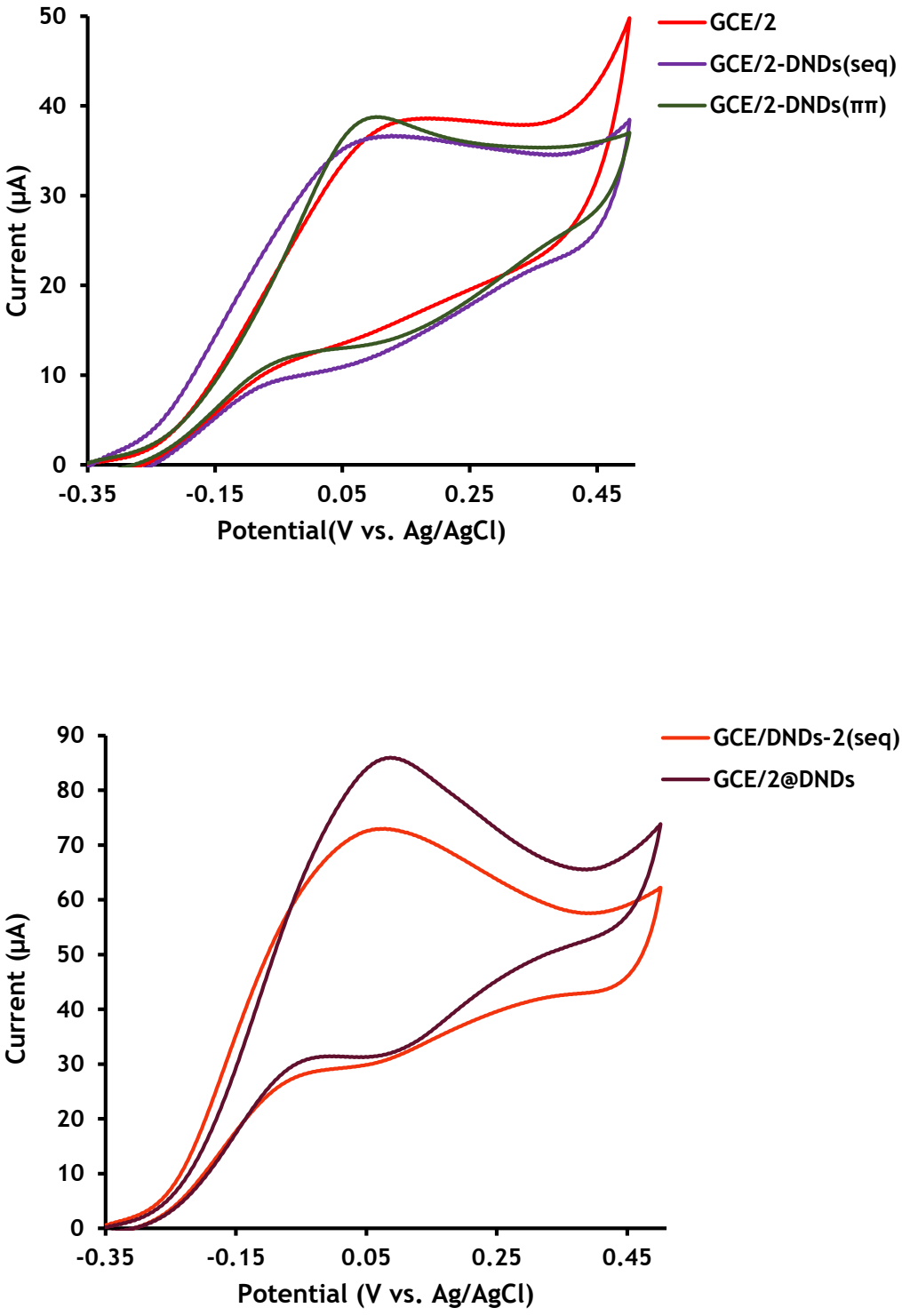

Figure 5.1: Cyclic voltammograms of bare GCE, GCE/DNDs, GCE/**1**, GCE/DNDs-**1**(seq), GCE/**1**-DNDs(seq), GCE/**1**-DNDs(ππ), GCE/**2**, GCE/DNDs-**2**(seq), GCE/**2**-DNDs(seq), GCE/**2**-DNDs(ππ) and GCE/CoPc@DNDs for the detection of 5 mM Hydrazine in 0.1 M sodium hydroxide at 90 mV/s scan rate.

Table 5.1: A summary of the electrocatalytic activity of modified electrodes towards 5 mM hydrazine in 0.1 M sodium hydroxide.

Electrodes	**Hydrazine oxidation potential/V**	**Backgroud corrected current/ μA**	**Tafel slopes (mV/decade**	**Γ (mol cm^{-2})**
Bare GCE	-	-	-	-
GCE/**1**	0.12	16	117	1.63×10^{-6}
GCE/DNDs	-	-	-	5.60×10^{-7}
GCE/DNDs-**1**(seq)	0.32	36	76	1.01×10^{-6}
GCE/**1**-DNDs(seq)	0.13	1.9	136	1.27×10^{-6}
GCE/**1**-DNDs(ππ)	0.25	24	194	7.13×10^{-7}
GCE/**2**	0.18	38	121	8.36×10^{-7}
GCE/DNDs-**2**(seq)	0.08	73	231	1.88×10^{-6}
GCE/**2**-DNDs(seq)	0.13	37	181	7.00×10^{-7}
GCE/**2**-DNDs(ππ)	0.14	38	173	4.59×10^{-7}
GCE/**2**@DNDs	0.09	86	67	1.53×10^{-6}

5.2 Kinetics

Kinetic studies were conducted by increasing the scan rates from 20 mV/s to 90 mV/s at a constant concentration of hydrazine, GCE/**2**@DNDs used as an example in **Fig. 5.2**. These studies were conducted to investigate the reversibility of the redox reaction on the modified electrode surfaces. **Figure 5.2(a)** shows that the oxidation reactions on the electrode surface are irreversible, because when the current increases, the potential shifts to the more positive side. The direct proportionality observed between current and square root of the scan rate at **Fig. 5.2 (b)** is a characteristic of a diffusion-controlled reaction. Furthermore, from the plot of log Ip vs. log v **Fig. 5.2(c)** the slope of the plot is close to 0.5 for both probes. These slopes are close to the theoretical value of a diffusion-controlled reaction (0.5) **[93]**.

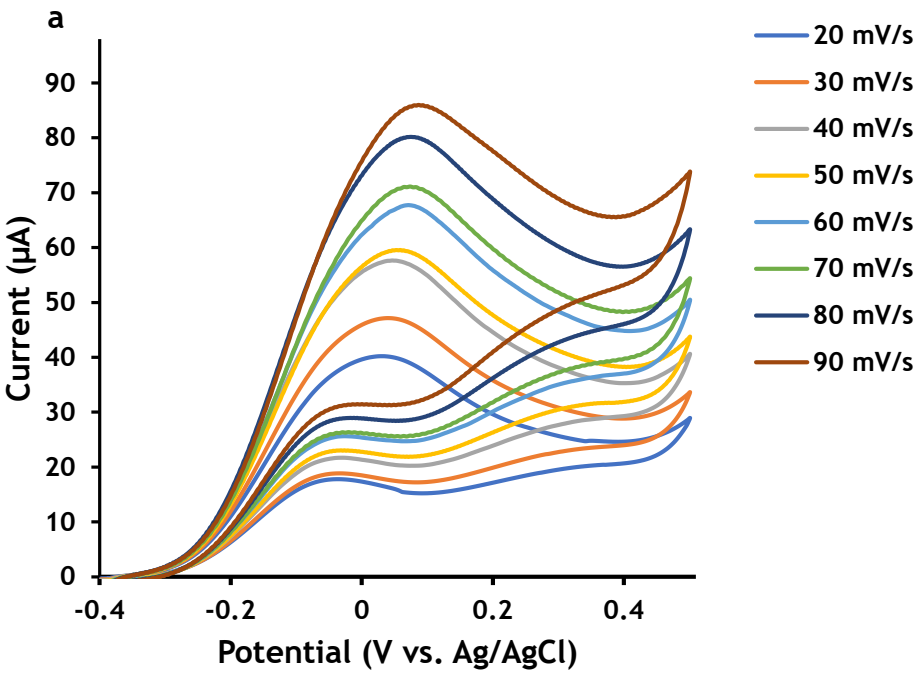

b

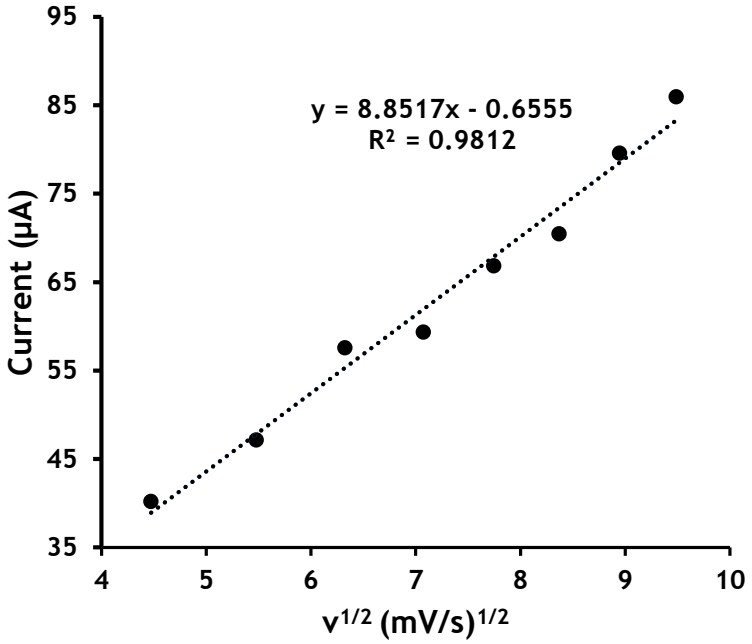
y = 8.8517x - 0.6555
R² = 0.9812
Current (µA)
95
85
75
65
55
45
35
4
5
6
7
8
9
10
v1/2 (mV/s)1/2

c

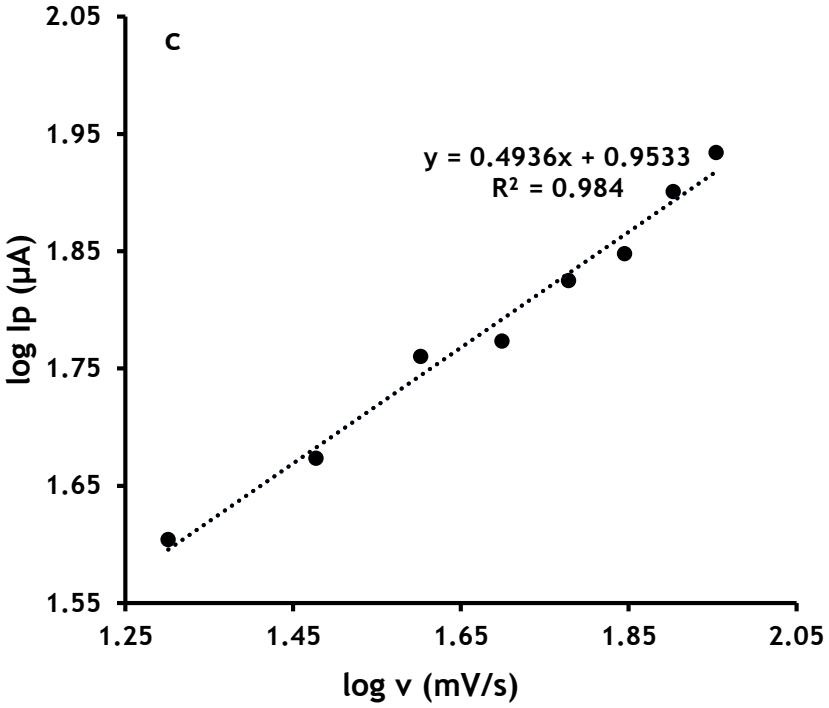
y = 0.4936x + 0.9533
R² = 0.984
log Ip (µA)
2.05
1.95
1.85
1.75
1.65
1.55
1.25
1.45
1.65
1.85
2.05
log v (mV/s)

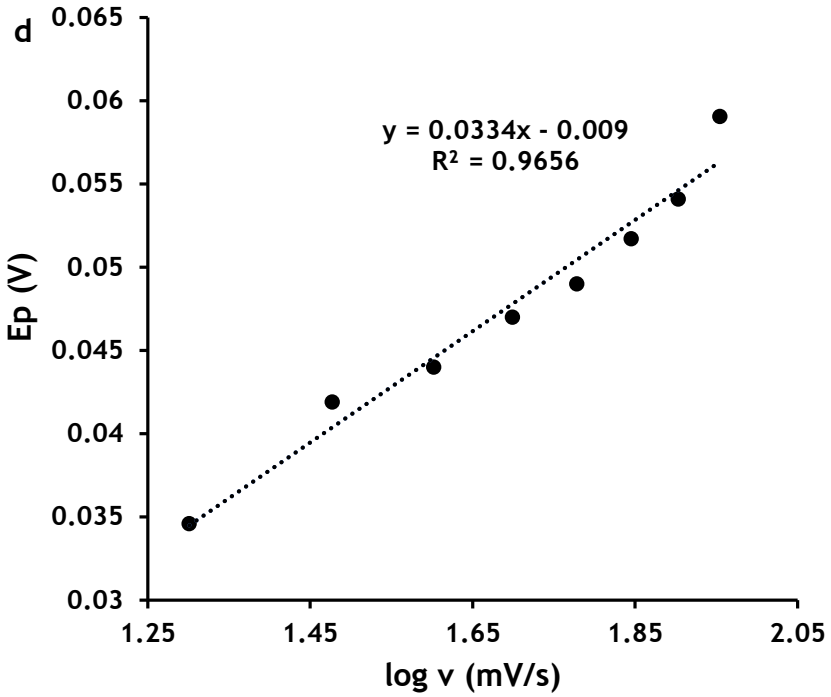

Figure 5.2: Cyclic voltammograms in 5 mM hydrazine in 0.1 M NaOH GCE/**2**@DNDs modified GCE at different scan rates 20 mV-90 mV, (a) multiple scan rates (b) plot of peak oxidation current vs square root of the scan rate, (c) log current vs log of scan rate and (d) potential (Ep) *vs* the logarithm of the scan rate (log *v*).

A further investigation of the processes happening on the electrode was carried by determining the Tafel slopes. The relationship of potential versus log of scan rates (log v) (**Fig.5.2a**) is given by **Equation 5.1** since the oxidation reaction is irreversible and diffusion-controlled **[94]**.

$$Ep = \frac{b}{2}\log v + K \qquad \textbf{(5.1)}$$

where *b* is the Tafel slope, *v* is scan rate and E_p is peak potential and *K* is a constant. Tafel slopes ranged from 67 to 231 mV/decade, **Table 5.1**. Tafel slopes outside the range of 60-120 mV/decade suggest the possibility of chemical complications on the

surface of the electrode, **[87,95]**. For GCE/**1**, GCE/DNDs-**1**(seq), GCE/**2**@DNDs and GCE/**2**, the Tafel slopes are within the 60-120 mV/decade range, but the rest fall outside this range (**Table 5.1**). Tafel slopes exceeding 120 mV/decade having no meaning in the kinetic sense **[87]**.

5.3 Stability studies

Stability studies were conducted for GCE/**2**@DNDs and GCE/**2** by running 10 consecutive scans in 5 mM hydrazine, **Fig. 5.3(a** and **b)**. The background corrected current for GCE/**2** decreased, whereas for GCE/**2**@DNDs it increased **Figure 5.3(a** and **b)**. The current increased by 3.9 % for GCE/**2**@DNDs, and decreased by 25 % for GCE/**2**. These results revealed that GCE/**2** was not stable, since the current kept on decreasing after 10 scans. In addition, the results from this study highlight an important role of detonation nanodiamonds in enhancing the electrocatalytic properties of phthalocyanines.

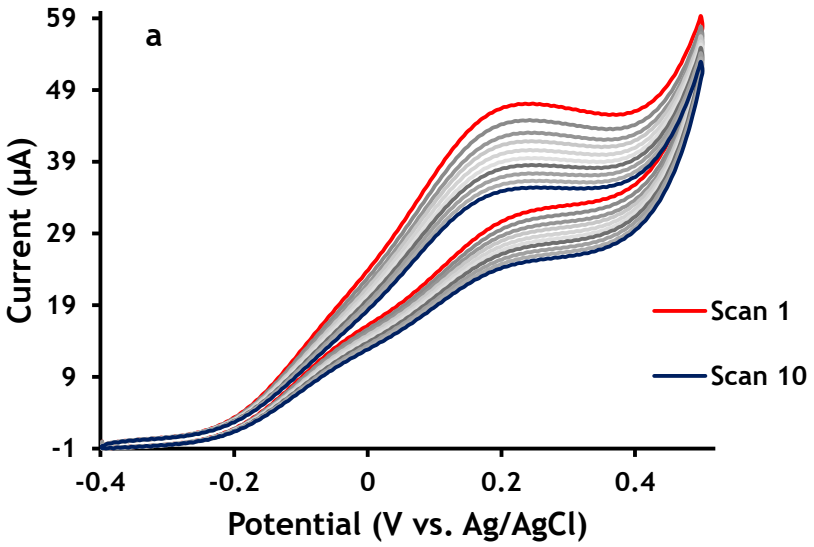

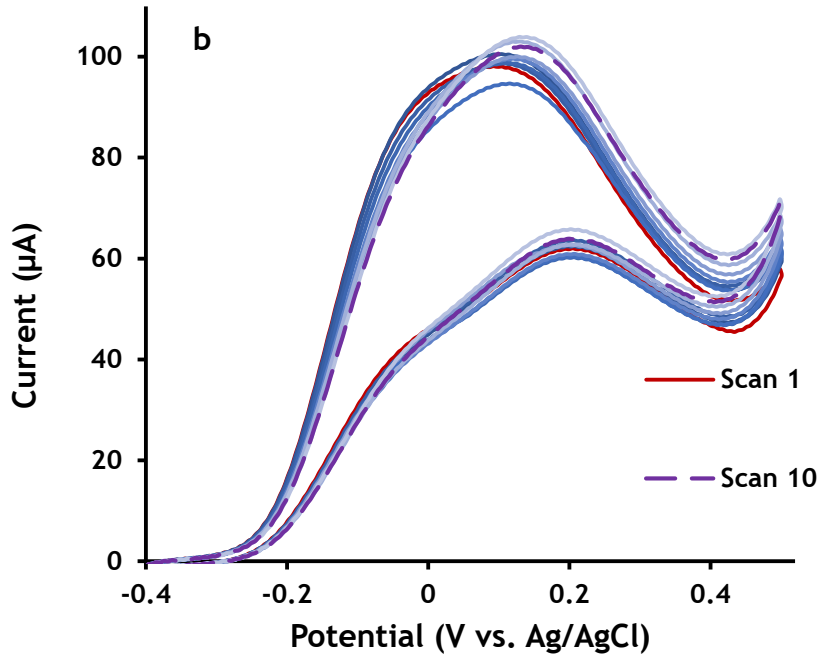

Figure 5.3: Cyclic voltammograms for stability studies on (a) GCE/**2** and (b) GCE/**2**@DNDs in 5 mM Hydrazine in 0.1 M NaOH at 90 mV/s.

5.4 Chronoamperometry

Limits of detection and catalytic rate constants (**Table 5.2**) were obtained using chronoamperometric experiments. **Figure 5.4(a)** illustrates chronoamperometry plots of GCE/**2**@DNDs as an example at varying concentrations (0.1-0.6 mM). Since bare GCE and GCE/DNDs did not show peaks in cyclic voltammogram, the chronoamerometry experiments were not conducted.

Table 5.2: A summary of chronoamperometric data for hydrazine electro-oxidation at different concentrations.

Electrodes	Catalytic rate constant ($M^{-1}. s^{-1}$)	Sensitivity	LoD (μM)	References
GCE/**1**	4.4×10^{5}	2.97	2.5	This work
GCE/DNDs-**1**(seq)	3.2×10^{3}	5.7	3.2	This work
GCE/**1**-DNDs(seq)	2.9×10^{2}	0.61	11	This work
GCE/**1**-DNDs(ππ)	1.3×10^{6}	9.6	1.7	This work
GCE/**2**	3.2×10^{3}	14	9.6	This work
GCE/DNDs-**2**(seq)	6.8×10^{4}	8.9	2.7	This work
GCE/**2**-DNDs(seq)	5.0×10^{4}	7.4	8.2	This work
GCE/**2**-DNDs(ππ)	1.6×10^{3}	0.46	13.5	This work
GCE/**2**@DNDs	9.3×10^{4}	11	0.33	This work
GCE/**3**-rGONs	1.37×10^{6}		0.82	**[96]**
GCE/**4**@NGQDs	4.31		6.81	**[39]**

rGONs = reduced graphene oxide nanosheets; NGQDs = Nitrogen doped graphene quantum dots; **3** = {tris *tert* butyl phenoxy mono [4-(4-(5-chloro-1H-benzo[d]imidazol-2-yl) phenoxy phthalocyaninato]} Co(II); **4** = 2,9,16-tris-(3-diethylamino)phenoxy) mono aminophenoxy phthalocyaninato Co(II).

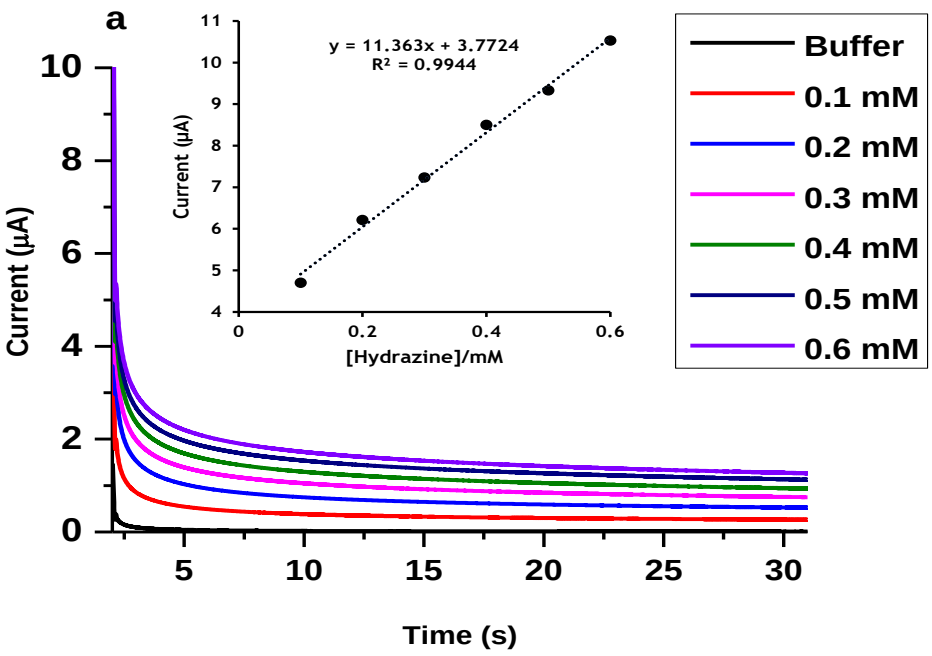
a
Current (μA)
Time (s)
y = 11.363x + 3.7724
R² = 0.9944
[Hydrazine]/mM
Buffer
0.1 mM
0.2 mM
0.3 mM
0.4 mM
0.5 mM
0.6 mM

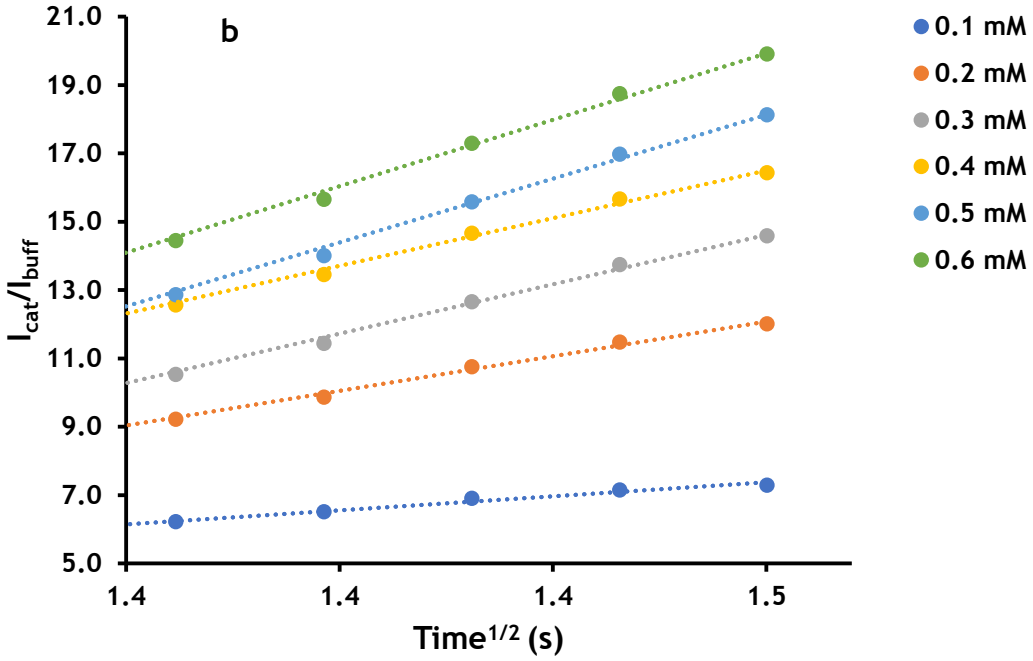
b
I_{cat}/I_{buff}
Time$^{1/2}$ (s)
0.1 mM
0.2 mM
0.3 mM
0.4 mM
0.5 mM
0.6 mM

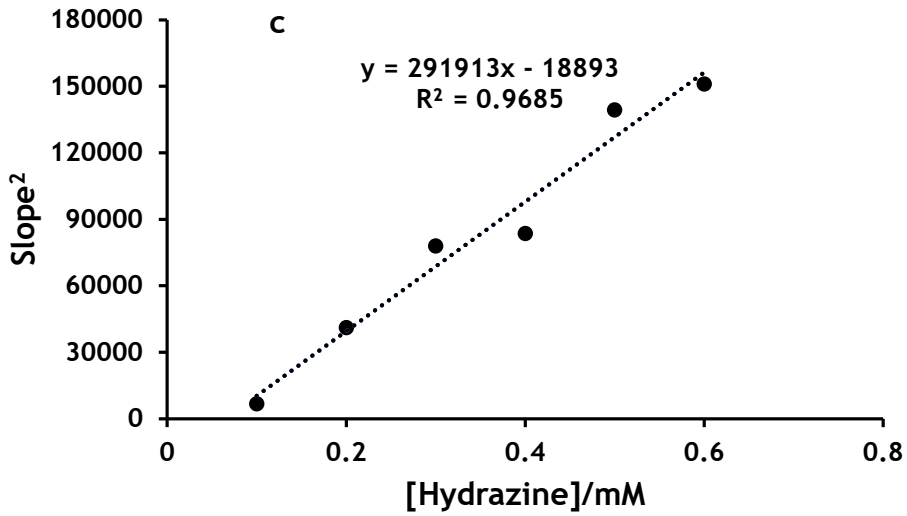

Figure 5.4: Chronoamperometry plots of GCE/**2**@DNDs at varying concentrations of hydrazine in 0.1 M NaOH (a) (insert calibration curve at t = 2 s), (b) plot of I_{cat}/I_{Buffer} vs. time$^{1/2}$, (c) plot of slope squared vs. hydrazine concentration.

The catalytic rate constants of the probes were calculated using the plot of I_{cat}/I_{buffer} versus square root of time (**Fig. 5.4(b)**) and according to the method described in literature **Eqn. 5.2 [97]**.

$$\frac{I_{cat}}{I_{buff}} = \pi^{1/2}(k_{cat}Ct)^{1/2} \qquad (5.2)$$

where I_{cat} and I_{buff} are currents in the presence and absence of hydrazine, respectively, C the concentration of hydrazine, k_{cat} is the catalytic rate constant and t as the time elapsed in seconds. The squared slopes in **(Fig. 5.4(b)**, were plotted against different the concentration of hydrazine **(Fg. 5.4(c)).** Slopes obtained from the linear plots are equal to πk_{cat} where k_{cat} is the catalytic rate constant ($M^{-1}s^{-1}$). A summary of rate constants is illustrated in **Table 5.2**.

The observations from obtained catalytic constants **(Table 5.2)** are:

- GCE/**2**@DNDs had the highest catalytic rate constant when compared to other probes.
- Sequentially modified electrodes revealed that when the CoPc is on top the probe performs better.
- The incorporation of DNDs to CoPc improved the catalytic rates of the CoPc, however it was not the case for GCE/**2**-DNDs(ππ), GCE/DNDs-**1**(seq) and GCE/**1**-DNDs(seq) . The behaviour may be attributed to phase separation between non-covalently linked nanosystems due to absence of a covalent bond between DNDs and CoPc. In addition to this, high catalytic rate of GCE/**2**@DNDs corresponds with the cyclic voltammetry **(Fig. 5.1)** data as it shows high background corrected current and lower potential **(Table 5.1)** when compared to other probes.

The limits of detection (LoD) were determined using 3δ/s, where δ is standard deviation of the blanks and s (sensitivity) from the slopes of the calibration **(Fig. 5.4(a) (Insert))**. A summary of LoDs illustrated in **Table 5.2,** reveals that GCE/**2**@DNDs had a lowest LoD of 0.33 μM and second highest sensitivity, LoD was better than some literature reports (**Table 5.2**) **[39,96]**. A look into sequentially modified electrodes GCE/DNDs-**2**(seq) and GCE/DNDs-**1**(seq) performed better than its counterparts GCE/**2**-DNDs(seq) and GCE/**1**-DNDs(seq), this shows the importance of placing the CoPc on top. The effectiveness of detonation nanodiamonds is observed in this study by decrease in LoDs except for GCE/**1**-DNDs(seq) and GCE/**2**-DNDs(ππ). The LoD is directly proportional to the catalytic rates of the probes, however it is not the case in some cases of this thesis.

5.5 Interference studies

The selectivity of GCE/**2**@DNDs probe towards hydrazine was studied in the presence of interferents (ammonia and aniline). In real life applications aniline and ammonia have a potential of interfering with hydrazine detection signals **[98]**, hence the exploration.The obtained data is shown in the form of square wave voltammograms in (**Fig. 5.5 a** and **b)**. The oxidation potentials for hydrazine + aniline and hydrazine+aniline+ammonia shifted to 0.19 V when compared to hydrazine alone (0.15 V). A decrease of 74 % in the current of hydrazine + ammonia was observed. In the presence of all three interferents current decreased by a huge percentage of 84 %. Even though there was a decrease, the electrode was still sensitive in the presence of both interferents, showing good electrocatalytic properties. The plots show peaks below 0.1 V which are not for analine and ammonia electrooxidation, this may be due to changes in conditions such as pH and temperature after the addition of interferents (**Fig. 5.5b**) **[99,100]**.

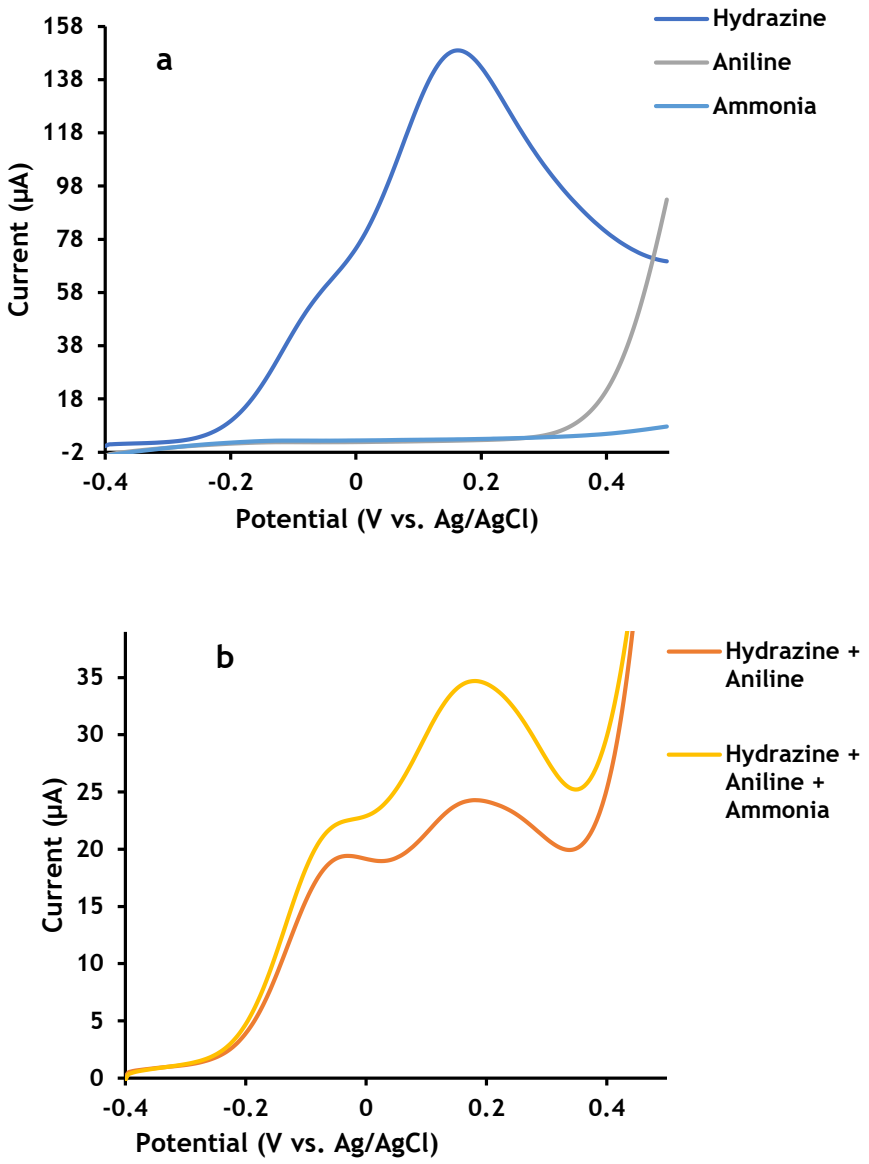

Figure 5.5: Square wave voltammograms of GCE/**2**@DNDs in **(a)** 5 mM hydrazine (H) pH 13.2, 10 mM aniline (A), 10 mM ammonia (AM), **(b)** hydrazine +aniline (H+A), hydrazine + ammonia (H+AM) and hydrazine + aniline + ammonia (H+A+AM) in 0.1 M NaOH.

5.6 Summary of the chapter

Modified electrodes showed successful electrooxidation towards hydrazine. The results obtained provide direction on the conjugation technique suitable for low detection limits. The covalently linked (GCE/**2**@DNDs) had the lowest LoD than other probes. Results also showed the importance of π-π stacking, since GCE/**1**-DNDs(ππ) had low LoD compared to sequentially modified electrodes, but for GCEs containing complex **2**, the symmetry lost activity in the presence of DNDs (GCE/**2**-DNDs(ππ). Combining nanomaterials with MPcs is known to give stable, sensitive and selective electrodes. This is proven in this chapter.

6 CONCLUSIONS AND FUTURE ASPECTS

Summary of the chapters discussed and future aspects are presented in this chapter

6.1 Conclusion

Novel symmetric and asymmetrical cobalt phthalocyanines are presented in this work. Thorough characterisation was performed on these complexes to confirm formation and purity. Spectroscopic techniques also confirmed the successful conjugation of complexes **1** and **2** to DNDs. The role of DNDs is noticeable in improving MPc's electrocatalytic properties towards hydrazine electrooxidation. In this work symmetry plays a significant role in electrocatalysis, since the obtained results show high sensitivity and current for GCE/**2**. In addition, asymmetrical phthalocyanine enabled covalent linkage. The covalently linked electrode GCE/**2**@DNDs was the best performing electrode. These observations show the importance of symmetry in phthalocyanines and conjugation via covalent linkage. Even though the GCE/**2**@DNDs recorded lower catalytic rate and sensitivity than some of the modified electrodes, however the probe recorded lowest limit of detection of 0.33 μM and second highest sensitivity, further highlighting nanomaterial's importance in the enhancement of electrocatalytic properties of MPcs.

6.2 Future aspects

Electrochemical studies on DNDs-MPc conjugates are represented in this thesis for the first time. There is huge gap in terms of combining different phthalocyanines with DNDs for electrochemical sensing, not only for hydrazine. Detonation nanodiamonds as carbon nanomaterial have tuneable properties. Doped carbon have been widely employed in electrocatalysis. This potential of DNDs can be extensively exploited in enhancing the properties of MPcs.

REFERENCES

1. B. V. Spitsyn and A. E. Alexenko, Chemical crystallization of diamond and the diamond coating deposition from gas phase. *Prot. Met.*, *43*, (2007) 431.
2. B. V. Spitsyn, S. A. Denisov, N. A. Skorik, A. G. Chopurova, S. A. Parkaeva, L. D. Belyakova, and O. G. Larionov, The physical–chemical study of detonation nanodiamond application in adsorption and chromatography. *Diam. Relat. Mater.*, *19*, (2010) 127.
3. A. M. Schrand, S. A. C. Hens, and O. A. Shenderova, Nanodiamond particles: properties and perspectives for bioapplications. *Crit. Rev. Solid State. Mater. Sci.*, *34*, (2009) 74.
4. L. Y. Bian, Y. H. Wang, J. B. Zang, F. W. Meng, and Y. L. Zhao, Detonation-synthesized nanodiamond as a stable support of Pt electrocatalyst for methanol electrooxidation. *Int. J. Electrochem. Sci.*, *7*, (2012) 7295
5. J. Zang, Y. Wang, L. Bian, J. Zhang, F. Meng, Y. Zhao, X. Qu, and S. Ren, Bucky diamond produced by annealing nanodiamond as a support of Pt electrocatalyst for methanol electrooxidation. *Int. J. Hydrog. Enegry*, 37, (2012) 6355.
6. M. Chipaux, K. J. van der Laan, S. R. Hemelaar, M. Hasani, T. Zheng, and R. Schirhagl, Nanodiamonds and their applications in cells. *Small*, *14*, (2018) 1704263.
7. T. S. Huang, Y. Tzeng, Y. K. Liu, Y. C. Chen, K. R. Walker, R. Guntupalli, and C. Liu, Immobilization of antibodies and bacterial binding on nanodiamond and carbon nanotubes for biosensor applications. *Diam. Relat. Mater.*, *13*, (2004) 1102.
8. J. Chen, M. Liu, Q. Huang, L. Huang, H. Huang, F. Deng, Y. Wen, J. Tian, X. Zhang, and Y. Wei, Facile preparation of fluorescent nanodiamond-based

polymer composites through a metal-free photo-initiated RAFT process and their cellular imaging. *Chem. Eng. J.*, *337*, (2018) 90.

9. L. Basso, M. Cazzanelli, M. Orlandi, and A. Miotello, Nanodiamonds: Synthesis and application in sensing, catalysis, and the possible connection with some processes occurring in space. *Appl. Sci.*, *10*, (2020) 4094.
10. W. Gu, N. Peters, and G. Yushin, Functionalized carbon onions, detonation nanodiamond and mesoporous carbon as cathodes in Li-ion electrochemical energy storage devices. *Carbon*, *53*, (2013) 301.
11. S. Saini, S. Sharma, M. Khangembam, and V. Singh, Nanodiamonds—Synthesis Techniques, Properties and Applications in Photovoltaics. In *Proceedings of the International Conference on Atomic, Molecular, Optical & Nano Physics with Applications* (2022) (137-153). Springer, Singapore.
12. J. X. Qin, X. G. Yang, C. F. Lv, Y. Z. Li, K. K. Liu, J. H. Zang, X. Yang, L. Dong, and C. X. Shan, Nanodiamonds: Synthesis, properties, and applications in nanomedicine. *Mater. Des.*, *210*, (2021) 110091.
13. C. Desai, K. Chen, S. Mitra, Aggregation behaviour of nanodiamonds and their functionalized analogs in an aqueous environment, *Environ. Sci. Processes Impact*, *16*, (2014) 523.
14. Y. Astuti, F.D. Saputra, S. Wuning, Arnelli, G. Bhaduri, Enrichment of Nanodiamond Surfaces with Carboxyl Groups for Doxorubicin Loading and Release. *Ser. Mater. Sci. Eng., 172,* (2017) 012066.
15. S. Osswald, G. Yushin, V. Mochalin, S.O. Kucheyev, Y. Gogotsi, Control of sp^2/sp^3 Carbon Ratio and Surface Chemistry of Nanodiamond Powders by Selective Oxidation in Air. *J. Am. Chem. Soc., 128,* (2006) 11642.

16. R. Matshitse, B. P. Ngoy, M. Managa, J. Mack, and T. Nyokong, Photophysical properties and photodynamic therapy activities of detonated nanodiamonds-BODIPY-phthalocyanines nanoassemblies. *Photodiagnosi. Photodyn. Ther., 26,* (2019) 110.
17. L. D. Dias, F. M. Rodrigues, M. J. Calvete, S. A. Carabineiro, M. D. Scherer, A. R. Caires, J. G. Buijnsters, J. L. Figueiredo, V. S. Bagnato, and M. M. Pereira, Porphyrin–Nanodiamond Hybrid Materials—Active, Stable and Reusable Cyclohexene Oxidation Catalysts. *Catalysts*, *10*, (2020) 1402.
18. S. A. Ansari, R. Satar, M. A. Jafri, M. Rasool, W. Ahmad, and S. K. Zaidi, Role of nanodiamonds in drug delivery and stem cell therapy. Iran. J. Biotechnol., *14*, (2016) 130.
19. C. G. Claessens, U. W. E. Hahn, and T. Torres, Phthalocyanines: From outstanding electronic properties to emerging applications. *Chem. Rec., 8,* (2008) 97.
20. M. C. DeRosa and R. J. Crutchley, Photosensitized singlet oxygen and its applications, *Coord. Chem. Rev., 233* (2002), 371
21. M. Urbani, M. E. Ragoussi, M. K. Nazeeruddin, and T. Torres, Phthalocyanines for dye-sensitized solar cells. *Coord. Chem. Rev., 381,* (2019) 64.
22. S. Pakapongpan, J. P. Mensing, D. Phokharatkul, T. Lomas, and A. Tuantranont, Highly selective electrochemical sensor for ascorbic acid based on a novel hybrid graphene-copper phthalocyanine-polyaniline nanocomposite. *Electrochim. Acta., 133,* (2014) 301.
23. S. Mgidlana, P. Şen, and T. Nyokong, Direct nonlinear optical absorption measurements of asymmetrical zinc (II) phthalocyanine when covalently

linked to semiconductor quantum dots. *J. Mol. Struct., 1220,* (2020) 128729.

24. S. S. Erdem, I. V. Nesterova, S. A. Soper, and R. P. Hammer, Solid-phase synthesis of asymmetrically substituted "AB3-type" phthalocyanines. *J. Org. Chem., 73,* (2008) 5007.
25. V. Nemykin, S. Dudkin, F. Dumoulin, C. Hirel, A. Gurek, and V. Ahsen, Synthetic approaches to asymmetric phthalocyanines and their analogues. *Arkivoc (1),* (2014) 204.
26. N. B. McKeown, Phthalocyanine-containing polymers. *J. Mater. Chem., 10,* (2000) 1995.
27. N. Kobayashi, H. Ogata, N. Nonaka, and E. A. Luk'yanets, Effect of peripheral substitution on the electronic absorption and fluorescence spectra of metal-free and zinc phthalocyanines. *Eur. J. Chem., 9,* (2003) 5134.
28. J. Mack, and N. Kobayashi, Low symmetry phthalocyanines and their analogues. *Chem. Rev., 111,* (2011) 321.
29. N. Nwaji, O. M. Bankole, J. Britton, and T. Nyokong, Photophysical and nonlinear optical study of benzothiazole substituted phthalocyanines in solution and thin films. *J. Porphyr. Phthalocyanines, 21,* (2017) 272.
30. J. Kim, E. Rajkumar, S. Kim, Y. M. Park, Y. Kim, S. J. Kim, and H. J. Lee, New cyclopentadienyl rhodium catalysts for electrochemical hydrogen production. *Catal. Today, 295,* (2017) 81.
31. P. Rajakumar, and V. Kalpana, Synthesis, photophysical and electrochemical properties of Fréchet type dienone core dendrimers with benzothiazole surface unit. *RSC Adv., 4,* (2014) 3788.

32. A. Begum, and P. G. Pickup, Electrocatalysis of CO2 reduction by ruthenium benzothiazole and bithiazole complexes. *Electrochem. Commun., 9*, (2007) 2528.
33. N. Jia, C. He, S. Wang, W. Song, Z. Chen, Y. Zu, Y. Gao, and Y. Dong, Effect of central metals and peripheral substituents on the third-order nonlinear optical properties of tetra-benzimidazole and benzothiazole substituted phthalocyanines. *Opt. Mater., 76*, (2018) 89.
34. J. H. Zagal, M. A. Gulppi, C. Depretz, and D. Lelièvre, Synthesis and electrocatalytic properties of octaalkoxycobalt phthalocyanine for the oxidation of 2-mercaptoethanol. *J. Porphyr. Phthalocyanines, 3*, (1999) 363.
35. L. S. Mpeta, P. Sen, and T. Nyokong, Investigation of electrocatalytic behaviour of low symmetry cobalt phthalocyanines when clicked to azide grafted carbon electrodes. *J. Electroanal. Chem., 860*, (2020) 113896.
36. E. Güzel, M. N. Yarasir, and A. R. Özkaya, Low symmetry solitaire-and trans-functional porphyrazine/phthalocyanine hybrid complexes: Synthesis, isolation, characterisation, and electrochemical and in-situ spectroelectrochemical properties. *Synth. Met., 262*, (2020) 116331.
37. Ö. A. Osmanbaş, A. Koca, I. Özçeşmeci, A. İ. Okur, and A. Gül, A., Voltammetric, spectroelectrochemical, and electrocatalytic properties of thiol-derivatized phthalocyanines. *Electrochim. Acta, 53*, (2008) 4980.
38. J. Britton, A. G. Martynov, D. O. Oluwole, Y. G. Gorbunova, A. Y. Tsivadze, and T. Nyokong, Improvement of nonlinear optical properties of phthalocyanine bearing diethyleneglycole chains: Influence of symmetry

lowering vs. heavy atom effect. *J. Porphyr. Phthalocyanines*, *20*, (2016) 1305.

39. R. Nkhahle, K. E. Sekhosana, S. Centane, and T. Nyokong, Electrocatalytic Activity of Asymmetrical Cobalt Phthalocyanines in the Presence of N Doped Graphene Quantum Dots: The Push-pull Effects of Substituents. *Electroanalysis*, *31*, (2019) 904.
40. L. C. Nene, and T. Nyokong, Photo-sonodynamic combination activity of cationic morpholino-phthalocyanines conjugated to nitrogen and nitrogen-sulfur doped graphene quantum dots against MCF-7 breast cancer cell line in vitro. *Photodiagnosis. Photodyn. Ther.*, *36*, (2021) 102573.
41. R. Matshitse, S. Khene, and T. Nyokong, Photophysical and nonlinear optical characteristics of pyridyl substituted phthalocyanine-detonation nanodiamond conjugated systems in solution. *Diam. Relat. Mater.*, *94*, (2019) 232.
42. R. Ghadari, P. S. Saei, A. Sabri, Z. Ghasemi, and F. Kong, Enhanced phthalocyanine-sensitized solar cell efficiency via cooperation of nitrogen-doped carbon dots. *J. Clean. Prod.*, *268*, (2020) 122236.
43. M. K. Barman, B. Jana, S. Bhattacharyya, and A. Patra, Photophysical properties of doped carbon dots (N, P, and B) and their influence on electron/hole transfer in carbon dots–nickel (II) phthalocyanine conjugates. *J. Phys. Chem. C.*, *118*, (2014) 20041.
44. W. Jiang, X. Chen, T. Wang, B. Li, M. Zeng, J. Yang, N. Hu, Y. Su, Z. Zhou, and Z. Yang, Enhancing room-temperature NO_2 gas sensing performance based on a metal phthalocyanine/graphene quantum dot hybrid material. *RSC Adv.*, *11*, (2021) 5628.

45. S. R. Nxele, and T. Nyokong, the electrochemical detection of prostate specific antigen on glassy carbon electrode modified with combinations of graphene quantum dots, cobalt phthalocyanine and an aptamer. *J. Inorg. Biochem.*, *221*, (2021) 111462.
46. T. Xu, D. Wang, L. Dong, H. Shen, W. Lu, and W. Chen, Graphitic carbon nitride co-modified by zinc phthalocyanine and graphene quantum dots for the efficient photocatalytic degradation of refractory contaminants. *Appl. Cat. B: Envir.*, *244*, (2019) 106.
47. Y. I. Openda, and T. Nyokong, Detonation nanodiamonds-phthalocyanine photosensitizers with enhanced photophysicochemical properties and effective photoantibacterial activity. *Photodiagnosis. Photodyn. Ther.*, *32*, (2020) 102072.
48. K. H. Koh, S. H. Noh, T. H. Kim, W. J. Lee, S. C. Yi, and T. H. Han, A graphene quantum dot/phthalocyanine conjugate: a synergistic catalyst for the oxygen reduction reaction. *RSC Adv.*, *7*, (2017) 26119.
49. L. Mao, X. Wang, Y. Guo, L. Yao, X. Xue, H. X. Wang, C. Xiong, W. Wen, X. Zhang, and S. Wang, A synergistic approach to enhance the photoelectrochemical performance of carbon dots for molecular imprinting sensors. *Nanoscale*, *11*, (2019) 7892.
50. S. Yang, Y. Yu, X. Gao, Z. Zhang and F. Wang, Recent advances in electrocatalysis with phthalocyanines, *Chem. Soc. Rev., 50,* (2021) 12985
51. T. Koczorowski, J. Kujawski, P. Bakun, L. Popenda, D. T. Mlynarczyk, P. Kleszcz, and S. Jurga, Electrochemical properties and electrocatalytic activity of novel iron and manganese tribenzopyrazinoporphyrazine complexes. *Synth. Met.*, *291*, (2022) 117193.

52. S. Chen, R. Yuan, Y. Chai, and F. Hu, Electrochemical sensing of hydrogen peroxide using metal nanoparticles: a review. *Micro. Acta.*, *180*, (2013) 32.
53. C. S. J. N. O'Donoghue, G. Fomo, T. Nyokong, Electrode modification using alkyne manganese phthalocyanine and click chemistry for electrocatalysis, *Electroanalysis*, 28, (2016) 3027.
54. R. Moscoso, J. Carbajo, and J. A. Squella, Multiwalled carbon nanotubes modified electrodes with encapsulated 1, 4-dihydro-pyridine-4-nitrobenzene substituted compounds. *J. Chil. Chem. Soc., 59*, (2014) 2501.
55. L. S. Koodlur, Layer-by-layer self-assembly of a water-soluble phthalocyanine on gold. Application to the electrochemical determination of hydrogen peroxide. *Bioelectrochemistry*, *91*, (2013) 27.
56. Y. Lu, and R. G. Reddy, The electrochemical behavior of cobalt phthalocyanine/platinum as methanol-resistant oxygen-reduction electrocatalysts for DMFC. *Electrochim. Acta*, *52*, (2007) 2569.
57. J. H. Zagal, S. Griveau, J. F. Silva, T. Nyokong, and F. Bedioui, Metallophthalocyanine-based molecular materials as catalysts for electrochemical reactions. *Coord. Chem. Rev.*, *254*, (2010) 2791.
58. N. N. Vershinin, O. N. Efimov, V. A. Bakaev, A. E. Aleksenskii, M. V. Baidakova, A. A. Sitnikova, and A. Y. Vul', Detonation nanodiamonds as catalyst supports. *Fuller. Nanotub. Carbon Nanostr.*, *19*, (2010) 68.
59. N. Gibson, O. Shenderova, T. J. M. Luo, S. Moseenkov, V. Bondar, A. Puzyr, K. Purtov, Z. Fitzgerald, and D. W. Brenner, Colloidal stability of modified nanodiamond particles. *Diam. Relat. Mater.*, *18*, (2009) 626.

60. N. B. Simioni, T. A. Silva, G. G. Oliveira, and O. Fatibello-Filho, A nanodiamond-based electrochemical sensor for the determination of pyrazinamide antibiotic. *Sens. Actuators B: Chem.*, *250*, (2017) 323.
61. S. Shahrokhian, and M. Ghalkhani, Glassy carbon electrodes modified with a film of nanodiamond–graphite/chitosan: Application to the highly sensitive electrochemical determination of Azathioprine. *Electrochim. Acta.*, *55*, (2010) 3627.
62. N. B. Simioni, G. G. Oliveira, F. C. Vicentini, M. R. Lanza, B. C. Janegitz, and O. Fatibello-Filho, Nanodiamonds stabilized in dihexadecyl phosphate film for electrochemical study and quantification of codeine in biological and pharmaceutical samples. *Diam. Relat. Mater.*, *74*, (2017) 196.
63. L. H. Chen, J. B. Zang, Y. H. Wang, and L. Y. Bian, Electrochemical oxidation of nitrite on nanodiamond powder electrode. *Electrochim. Acta.*, *53*, (2008) 3445.
64. A. Poso, A. von Wright, and J. Gynther, An empirical and theoretical study on mechanisms of mutagenic activity of hydrazine compounds. *Mutat. Res. - Fundam. Mol. Mech.*, *332*, (1995) 71.
65. T. Kean, J. H. Miller, G. G. Skellern, and D. Snodin, Acceptance criteria for levels of hydrazine in substances for pharmaceutical use and analytical methods for its determination. *Pharmeur. Sci. Notes*, *2*, (2006) 33.
66. F. A. Harraz, A. A. Ismail, S. A. Al-Sayari, A. Al-Hajry, and M. S. Al-Assiri, Highly sensitive amperometric hydrazine sensor based on novel α-Fe2O3/crosslinked polyaniline nanocomposite modified glassy carbon electrode. *Sens. Actuators. B. Chem.*, *234*, (2016) 582.

67. A. Mohammad, M. E. Khan, and M. H. Cho, Sulfur-doped-graphitic-carbon nitride (Sg-C3N4) for low-cost electrochemical sensing of hydrazine. *J. Alloys. Compd., 816,* (2020) 152522.
68. Y. Y. Tang, C. L. Kao, and P. Y. Chen, Electrochemical detection of hydrazine using a highly sensitive nanoporous gold electrode. *Anal. Chim. Acta., 711,* (2012) 39.
69. H. Zhang, J. Huang, H. Hou, and T. You, Electrochemical detection of hydrazine based on electrospun palladium nanoparticle/carbon nanofibers. *Electroanalysis, 21,* (2009) 1874.
70. D. A. Venegas-Yazigi, G. I. Cárdenas-Jirón, and J. H. Zagal, Theoretical study of the electron transfer reaction of hydrazine with cobalt (II) phthalocyanine and substituted cobalt (II) phthalocyanines. *J. Coord. Chem., 56,* (2003) 1275.
71. M. S. Ağirtaş, U. J. Yildiko, Synthesis of new phthalocyanines substituted with four benzo[d]thiazol-2-ylthio groups. *Coord. Chem., 61,* (2008) 2786.
72. O. Yıldırım, A. M. Sevim, and A. Gül, Novel water-soluble metallophthalocyanines supported on cotton fabric. *Colora. Techn., 128,* (2012) 243.
73. R. Matshitse, M. Managa, T. Nyokong, The modulation of the photophysical and photodynamic therapy activities of a phthalocyanine by detonation nanodiamonds: Comparison with graphene quantum dots and carbon nanodots. *Diam. Relat. Mater., 101,* (2020) 1076172.
74. J. Rusanova, M. Pilkington, S. Decurtins, A novel fully conjugated phenanthroline-appended phthalocyanine: synthesis and characterisation, Chem. Comm. *19,* (2002) 2237.

75. G. Fomo, N. Nwaji, T. Nyokong, Low symmetric metallophthalocyanine modified electrode via clickchemistry for simultaneous detection of heavy metals, *J. Electroanal. Chem., 813,* (2018) 66.
76. B. Böttger and U. Schindewolf, Preparation and Polymorphism of Thin Films of Unsubstituted Cobalt Phthalocyanine. *Langmuir, 14,* (1998) 5194.
77. T. Furuyama, T. Ishii, N. Leda, H. Maeda, M. Segi, M. Uchiyama, H. Nakagawa, Cationic axial ligands on sulfur substituted silicon(IV) phthalocyanines: improved hydrophilicity and exceptionally red-shifted absorption into the NIR region. *Chem. Commun., 55,* (2019) 7314.
78. Z. D. Liu, H. X. Zhao, and C. Z. Huang, Obstruction of photoinduced electron transfer from excited porphyrin to graphene oxide: a fluorescence turn-on sensing platform for iron (III) ions. *PLoS One*, *7*(12), (2012) 50367.
79. M. J. Stillman, T. Nyokong, Phthalocyanines: properties and applications. New York, 1, (1989) 133. C. C. Leznoff, and A. B. P. Lever, A.B.P.
80. B. Lorber, F. Fischer, M. Bailly, H. Roy, D. Kern, Protein Analysis by Dynamic Light Scattering: Methods and Techniques for Students, *Biochem. Mol. Bio., 40,* (2012) 382
81. Z. Li, C. He, Z. Wang, Y. Gao, Y. Dong, C. Zhao, Z. Chen, Y. Wu, W. Song, Ethylenediamine-modified graphene oxide covalently functionalized with a tetracarboxylic Zn (ii) phthalocyanine hybrid for enhanced nonlinear optical properties. *Photochem. Photobio. Sci., 15,* (2016) 919.
82. V. I. Korepanov, H. Hamaguchi, E. Osawa, V. Ermolenkov, I. K. Lednev, B. J.M. Etzold, O. Levinson, B. Zousman, C. P. Epperla, H.-C. Chang, Carbon

structure in nanodiamonds elucidated from Raman spectroscopy, *Carbon 121*, (2017) 329

83. O. Bajjou, M. Khenfouch, M. Baïtoul, B. Mothudi, M. Dhlamini, E. Faulques, and M. Maaza, Vibrational and optical properties of Meso-tetrakis (4-phenylsulfonica-acid) porphyrin decorated with graphene oxide. In IOP Conference Series: *Mater. Scie. Engin., 186,* (2017). IOP Publishing, 012003
84. F. J. Rawson, A. J. Downard, and K. H. Baronian, Electrochemical detection of intracellular and cell membrane redox systems in Saccharomyces cerevisiae. *Sci. Rep., 4,* (2014) 9.
85. A. H. Suroviec, Determining surface coverage of self-assembled monolayers on gold electrodes. *Chem. Educ., 17*, (2012) 85.
86. J. J. Gooding, V. G. Praig, and E. A. H. Hall, Platinum-catalyzed enzyme electrodes immobilized on gold using self-assembled layers. *Anal. Chem., 70*, (1998) 2402.
87. C. A. Caro, F. Bedioui, J. H. Zagal, Electrocatalytic oxidation of nitrite on a vitreous carbon electrode modified with cobalt phthalocyanine. *Electrochim. Acta., 47,* (2002) 1494.
88. V. Mani, R. Devasenathipathy, S. M. Chen, S. T. Huang, V. S. Vasantha, Immobilization of glucose oxidase on graphene and cobalt phthalocyanine composite and its application for the determination of glucose. *Enzy. Microbial. Techno., 66,* (2014) 66.
89. N. Hashemzadeh, M. Hasanzadeh, N. Shadjou, J. Eivazi-Ziaei, M. Khoubnasabjafari, and A. Jouyban, Graphene quantum dot modified glassy carbon electrode for the determination of doxorubicin hydrochloride in human plasma, *J. Pharma. Anal., 6,* (2016) 241.

90. A. H. Suroviec, Determining surface coverage of self-assembled monolayers on gold electrodes. *Chem. Educ*, *17*, (2012) 85.
91. Z. Li, M. Lieberman, and W. Hill, XPS and SERS study of silicon phthalocyanine monolayers: umbrella vs octopus design strategies for formation of oriented SAMs. *Langmuir*, *17*, (2001) 4894.
92. I. G. Casella, and M. Contursi, Electrocatalytic Oxidation of Some Hydrazine Compounds at Glassy Carbon Electrode Modified with Co-Gluconate Complex. *Electroanalysis*, *24*, (2012) 758.
93. S. N. Azizi, S. Ghasemi, and E. Chiani, Nickel/mesoporous silica (SBA-15) modified electrode: an effective porous material for electrooxidation of methanol. *Electrochim. Acta.*, *88*, (2013) 472.
94. A. Salimi, K. Abdi, Enhancement of the analytical properties and catalytic activity of a nickel hexacyanoferrate modified carbon ceramic electrode prepared by two-step sol–gel technique: application to amperometric detection of hydrazine and hydroxyl amine. *Talanta, 63,* (2004) 483.
95. J. M. Zen, A. S. Kumar, and M. R. Chang, Electrocatalytic oxidation and trace detection of amitrole using a Nafion/lead–ruthenium oxide pyrochlore chemically modified electrode. *Electrochim. Acta., 45*, (2000) 1700.
96. L. S. Mpeta, P. Sen, and T. Nyokong, The effects of asymmetry in combination with reduced graphene oxide nanosheets on hydrazine electrocatalytic detection on cobalt phthalocyanines. *Electroanalysis*, *32*, (2020) 2732.
97. H. Karimi-Maleh, M. Moazampour, A. A. Ensafi, S. Mallakpour, and M. Hatami, An electrochemical nanocomposite modified carbon paste electrode as a sensor for simultaneous determination of hydrazine and

phenol in water and wastewater samples. *Environ. Sci. Pollut. Res.,* (9), (2014) 5888.

98. A. N. Koreshkova, V. Gupta, A. Peristyy, P. N. Nesterenko, T. Rodemann, and B. Paull, Ion chromatographic determination of hydrazine in excess ammonia for monitoring graphene oxide reduction reaction. *Talanta*, *205*, (2019) 120081.

99. E. M. Farber, K. Ojha, T. Y. Burshtein, and D. Eisenberg, Carbon electrocatalysts for hydrazine oxidation: self-templating design of hierarchical porosity using barium carbonate nanoparticles. *J. Electrochem. Soc.*, *167*, (2020) 064517.

100. A. C. Arulrajan, C. Renault, and S. C. Lai, How changes in interfacial pH lead to new voltammetric features: the case of the electrochemical oxidation of hydrazine. *Phys. Chem. Chem. Phys.*, *20*, (2018) 11793.

Appendix

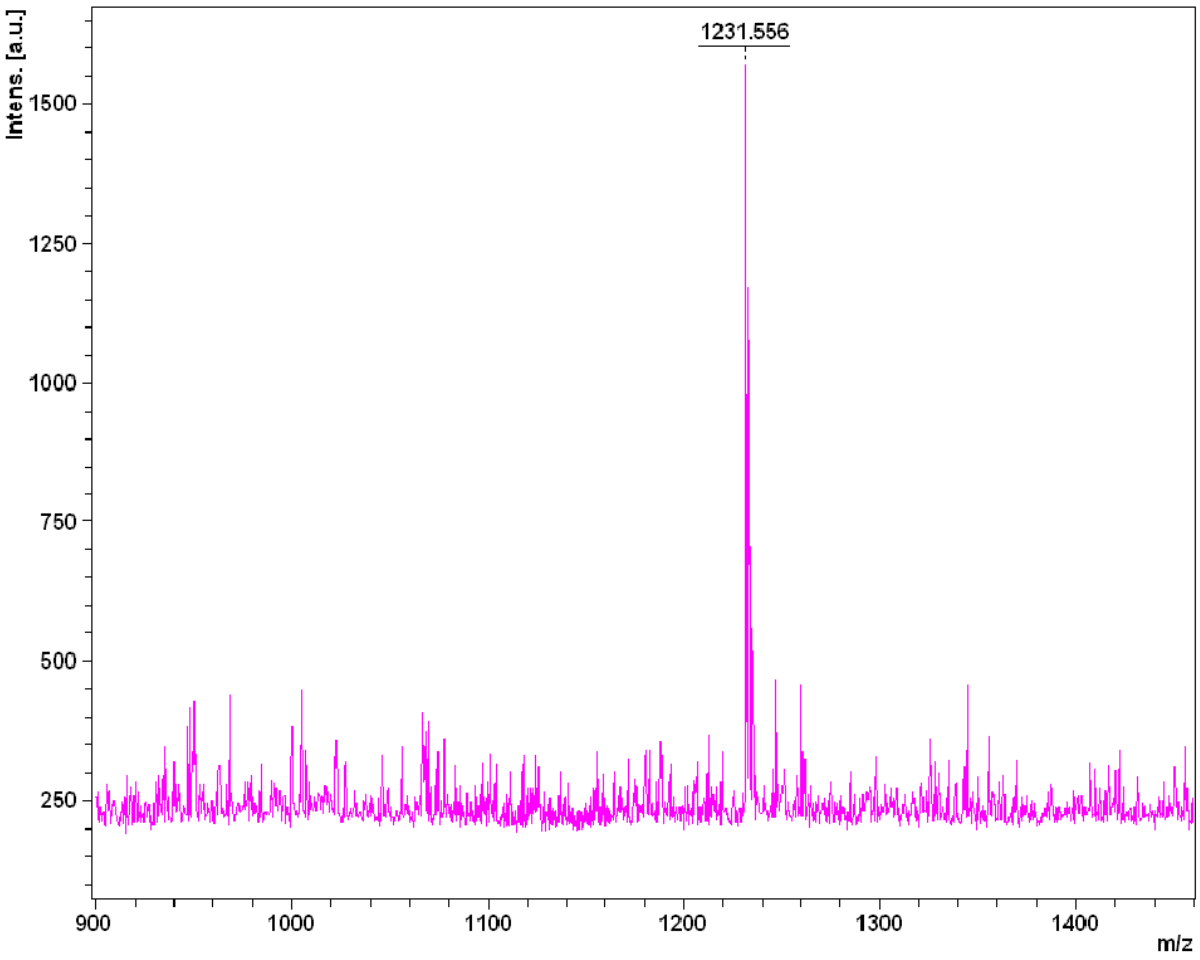

Figure A1: Mass spectra for complex **1**.

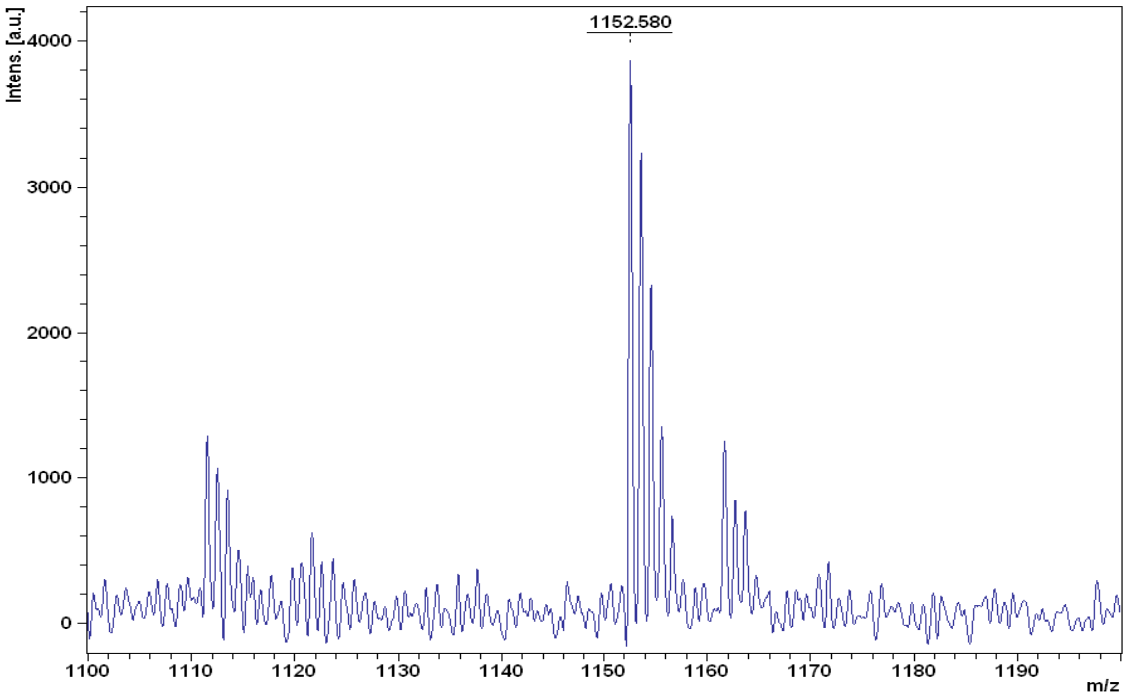

Figure A2: Mass spectra for complex **2.**